

# Cold giant discoveries from a joint radial-velocity and astrometry framework

## EMPEROR II – Jupiter analogues around metal-rich CHEPS stars

Pablo A. Peña<sup>1,2,\*</sup>, James S. Jenkins<sup>1,2</sup>, Fabo Feng<sup>3</sup>, Douglas R. Alves<sup>1,2</sup>, Florence de Almeida<sup>1</sup>, Frédéric Dux<sup>4</sup>, Guang-Yao Xiao<sup>3</sup>, Joanne M. Rojas M.<sup>1,2</sup>, Jose I. Vines<sup>5</sup>, Rafael I. Rubenstein<sup>1,6</sup>, R. Ramírez Reyes<sup>2,7</sup>, Suman Saha<sup>1,2</sup>, Connor J. Cheverall<sup>1,2</sup>, and Matías R. Díaz<sup>8</sup>

<sup>1</sup> Instituto de Estudios Astrofísicos, Facultad de Ingeniería y Ciencias, Universidad Diego Portales, Av. Ejército 441, Santiago, Chile

<sup>2</sup> Centro de Astrofísica y Tecnologías Afines (CATA), Casilla 36-D, Santiago, Chile

<sup>3</sup> State Key Laboratory of Dark Matter Physics, Tsung-Dao Lee Institute & School of Physics and Astronomy, Shanghai Jiao Tong University, Shanghai 201210, PR China

<sup>4</sup> Institute of Physics, Laboratory of Astrophysics, École Polytechnique Fédérale de Lausanne (EPFL), Observatoire de Sauverny, 1290 Versoix, Switzerland

<sup>5</sup> Instituto de Astronomía, Universidad Católica del Norte, Angamos 0610, 1270709, Antofagasta, Chile

<sup>6</sup> United States Fulbright Fellow; Chile Fulbright Commission, Chile

<sup>7</sup> Instituto de Astrofísica, Departamento de Física y Astronomía, Facultad Ciencias Exactas, Universidad Andrés Bello, Fernández Concha 700, Las Condes, Santiago, Chile

<sup>8</sup> Las Campanas Observatory, Carnegie Institution for Science, Raul Bitrán 1200, La Serena, Chile

Received 2 November 2025 / Accepted 11 March 2026

### ABSTRACT

**Context.** The population of long-period giant planets shapes planetary system architectures and formation pathways, but these cold Jupiters remain relatively unexplored. Radial velocity (RV) surveys lose sensitivity at multi-AU separations and provide only minimum planet masses, while the detection probability of transit surveys at long periods is low. Absolute astrometry from the HIPPARCOS and *Gaia* missions offers an additional source for stellar motion that can break the orbital inclination degeneracy and strengthen detection confidence. This is especially timely ahead of *Gaia* DR4 and DR5, which is expected to enable routine astrometric vetting and true-mass measurements for long-period RV planets.

**Aims.** Extending the Chile-Hertfordshire ExoPlanet Survey (CHEPS) by combining RVs spanning up to 16 years with absolute astrometry, we search for and characterise cold giants around metal-rich FGK stars.

**Methods.** We upgraded the EMPEROR framework by incorporating astrometric differencing to jointly fit RVs and astrometry for five CHEPS targets, and we performed a Bayesian model comparison and baseline- and phase-coverage metrics to quantify the astrometric contribution.

**Results.** Our analysis confirms and characterises orbital parameters for two known planets in HIP 21850 and detects five new planets: a warm Jupiter, HIP 10090c, with an orbital period  $P = 321.8^{+0.3}_{-0.6}$  d and mass  $M = 0.85^{+0.03}_{-0.12} M_J$ , and four Jupiter analogues, HIP 8923b with  $P = 14.1^{+0.4}_{-0.7}$  yr and  $M = 9.98^{+0.78}_{-0.16} M_J$ , HIP 10090b with  $P = 8.1^{+0.3}_{-0.3}$  yr and  $M = 3.87^{+0.65}_{-0.60} M_J$ , HIP 39330b with  $P = 12.7^{+0.6}_{-0.7}$  yr and  $M = 1.68^{+0.16}_{-0.13} M_J$ , and HIP 98599b with  $P = 7.3^{+0.1}_{-0.1}$  yr and  $M = 6.85^{+0.10}_{-0.22} M_J$ . The addition of astrometry reduces the period and mass uncertainties by factors between 3 and 10 whilst increasing the Bayes factors by up to  $\sim 60$ .

**Conclusions.** The synergy of long-baseline RVs and absolute astrometry provides a robust pathway for discovering and characterising cold giant planets and metal-rich Solar System analogues. Our results demonstrate that astrometric samples meaningfully improve detection confidence and convert minimum masses into true masses. This approach fills the demographic gap between RV and direct-imaging sensitivities and prepares the field for forthcoming astrometric missions that will allow us to find stellar systems like our own.

**Key words.** methods: data analysis – methods: statistical – techniques: radial velocities – astrometry – planets and satellites: detection – planetary systems

## 1. Introduction

Metal-rich stars have played a central role in exoplanet discovery since the earliest detections of gas giants, and the planet-metallicity correlation remains one of the most robust demographic trends: gas giants are markedly more common around metal-rich FGK stars (Gonzalez 1997; Santos et al. 2004;

Fischer & Valenti 2005; Winn 2018). Today, there are over 6000 confirmed exoplanets, the vast majority found by radial velocities (RVs) and transit photometry. However, the sensitivity of both techniques declines with orbital separation  $a$  (Zhu & Dong 2021): the geometric transit probability scales as  $R_\star/a$ , and long-period RV signals require many years of high-precision monitoring to resolve slowly varying signals with a low amplitude (Cumming et al. 2008). As a result, the population of cold-orbiting giants beyond a few AU remains comparatively unexplored.

\* Corresponding author: astro.reddtea@gmail.com

When we refer to exoplanets here, we adopt the term ‘cold’ for those with a semi-major axis of 1–10 AU, ‘wide-orbiting’ for >10 AU, and ‘Jupiter analogue’ for 3–7 AU and a mass of 0.3–13  $M_J$  (Bryan et al. 2019). Recent occurrence-rate analyses showed that Jupiters with orbital periods >100 d occur around Sun-like stars at 6–7%. They are more common by nearly an order of magnitude than hot Jupiters (Wittenmyer et al. 2020). Moreover, the relative occurrence of hot to cold Jupiters appears to decrease with stellar mass, consistent with expectations from classical core accretion and migration timescales (Gan et al. 2024). These trends highlight the need for long-baseline surveys capable of detecting and characterising cold giants.

While precise RVs constrain orbital parameters and minimum masses  $M_{\text{pl}} \sin i$ , they do not measure inclination, and thus, they cannot yield true masses by themselves. Absolute astrometry, on the other hand, is directly sensitive to the sky-projected stellar reflex motion and provides dynamical masses and inclinations, albeit with sensitivity that degrades with distance  $d$ . In particular, the signal-to-noise ratio (S/N) scales as  $S/N_{\text{AM}} \propto \frac{M_{\text{pl}} \cdot a}{M_* \cdot d}$ , while for RVs, this ratio scales as  $S/N_{\text{RV}} \propto \frac{M_{\text{pl}}}{\sqrt{a \cdot M_*}}$ .

Combining RVs with absolute astrometry breaks key degeneracies, enhances the S/N, and enables a robust characterisation of long-period companions even when a single technique samples only a fraction of the orbit. With HIPPARCOS (Hipp) and *Gaia* providing high-precision positions, proper motions, and accelerations over a baseline of  $\sim 24$  yr, the RV+astrometry synergy has matured to a powerful pathway for measuring true masses of cold giants and identifying a precise dynamical mass for Jupiter analogues (Perryman et al. 2014; Kervella et al. 2022; Feng et al. 2019; Brandt 2021).

A paradigm shift is imminent within the precision-RV community: long-period RV candidates will increasingly be treated as testable astrometric hypotheses and systematically checked for consistency with *Gaia*. In practice, an RV posterior predicts an on-sky reflex signal (amplitude and orientation) that *Gaia* can confirm, refute, or tighten into a true-mass measurement. Recent forecasts suggest that *Gaia* astrometry may yield  $7500 \pm 2100$  planet detections in DR4 and  $120\,000 \pm 22\,000$  in DR5, with  $\sim 1900 \pm 540$  (DR4) and  $38\,000 \pm 7300$  (DR5) having masses and periods measured to be better than 20%. Most of these detections are expected to be super-Jupiters on  $\sim 2$ –5 AU orbits around nearby GKM stars (Lammers & Winn 2026), overlapping with the parameter space targeted by long-baseline Doppler surveys.

The connection between outer cold giants and small inner planets is crucial for understanding system architectures. Early observational work reported that systems with inner super-Earths frequently host cold giants (roughly one in three), implying a positive correlation (Zhu et al. 2018; Bryan et al. 2019). Subsequent studies found lower conditional rates or no excess in carefully vetted samples (Bonomo et al. 2023). A more nuanced, mass-dependent picture is emerging: new analyses indicate that Saturn-mass cold giants are positively correlated with inner super-Earths, whilst the most massive super-Jupiters are not, potentially reconciling previous discrepancies and informing models of accretion efficiency and dynamical histories in multi-planet systems (Lefèvre-Forján & Mulders 2025). Establishing how common true Jupiter analogues are and measuring their dynamical masses directly bears on how typical the Solar System is among planetary systems.

Cold giants regulate the assembly and survival of inner planetary systems, sculpt debris belts, and provide boundary conditions for planet formation theories (migration histories, core accretion Ida et al. 2013; Mordasini et al. 2012). Measuring their occurrence, mass function, and orbital architectures tests these theories where they differ most, informs the demographics accessible to direct imaging, and provides prime targets for follow-up. The newly developed RV-astrometry coupling is explicitly built into future facilities: the Tianyu transit project plans confirmation and characterisation of long-period giants via *Gaia* astrometry and RV follow-up, leveraging multi-survey baselines (Feng et al. 2024b); and Habitable Worlds Observatory (HWO; Dressing et al. 2024) studies emphasise that precursor RVs together with a modest number of astrometric epochs can deliver full orbital solutions for cold giants and habitable-zone planets, enabling efficient direct-imaging campaigns (Sagynbayeva et al. 2025).

The Chile-Hertfordshire ExoPlanet Survey (CHEPS) was initiated in 2009 to target inactive, metal-rich stars with high-precision RVs from HARPS and CORALIE, explicitly leveraging the planet-metallicity correlation to find gas giants efficiently (Jenkins et al. 2008, 2009, 2017). By extending the CHEPS observations through 2025, we assembled a 16-year time baseline (2009–2025) ideally suited to unveil long-period curvatures and complete (or near complete) orbits for cold exoplanets. In this paper, we leverage this long CHEPS baseline with modern astrometric constraints. We (1) identify five CHEPS targets exhibiting long-term RV curvature (HIP 8923, HIP 10090, HIP 21850, HIP 39330, and HIP 98599); (2) model each system with a joint RV+astrometry framework using EMPEROR (Peña R & Jenkins 2026); and (3) determine the true masses and orbital parameters of the suspected cold giants. Beyond target-level results, our analysis serves as an end-to-end validation for the EMPEROR approach for combined RV+astrometry inference on long period planets. The paper is organised as follows: Sect. 2 outlines the joint modelling framework; Sect. 3 summarises datasets and stellar parameters; Sect. 4 presents system-by-system fits; Sect. 5 discusses and quantifies the benefits of the joint modelling, places the discovered systems in the context of the overall exoplanetary census, and addresses possible drawbacks in this study; and Sect. 6 summarises the key points of this research.

## 2. Overview of the modelling framework

EMPEROR (Exoplanet Mcmc Parallel tEmpering for Rv Orbit Retrieval; Peña R & Jenkins 2026) is a modular Python-based pipeline that searches RV time series for planetary signals and performs Bayesian model comparison to select the preferred solution. Posteriors are sampled with reddemcee (Peña R & Jenkins 2026), an adaptive parallel tempering (APT) MCMC sampler (Earl & Deem 2005; Vousden et al. 2016) designed to explore broad multi-modal posteriors efficiently and mitigate local trapping, significantly accelerating convergence rates while improving the reliability of global inferences. The framework estimates the marginalised likelihood (also known as evidence) through a hybrid approach that combines thermodynamic integration (Gelman & Meng 1998) and stepping stones (SS, Xie et al. 2011) with realistic uncertainties. EMPEROR supports multi-instrument, multi-planet analyses, and flexible noise models including (when needed) stellar activity correlations and Gaussian processes. In what follows, we summarise the Bayesian formulation and models

used, and describe how we incorporated the HIPPARCOS-*Gaia* differencing framework in the joint likelihood (Feng et al. 2019).

### 2.1. Bayesian formulation

The Bayes theorem defines the posterior  $p(\boldsymbol{\theta} | D, M)$  of parameters  $\boldsymbol{\theta}$ , given data  $D$  and model  $M$  as

$$p(\boldsymbol{\theta} | D, M) = \frac{p(\boldsymbol{\theta} | M) \cdot p(D | \boldsymbol{\theta}, M)}{p(D | M)}, \quad (1)$$

where  $p(\boldsymbol{\theta} | M)$  is the prior,  $p(D | \boldsymbol{\theta}, M)$  the likelihood, and  $p(D|M)$  the Bayesian evidence normalising the posterior (Robert 2007; Fong & Holmes 2019; Lotfi et al. 2022). The evidence enables objective model comparison via Bayes' factors. In our case, the likelihood is joint, coupling RVs and astrometry (subscript AM) through the shared orbital parameters  $\boldsymbol{\theta}$ ,

$$p(D | \boldsymbol{\theta}, M) = p(D_{\text{RV}} | \boldsymbol{\theta}, M) \times p(D_{\text{AM}} | \boldsymbol{\theta}, M). \quad (2)$$

### 2.2. Radial velocity model

The deterministic RV signal is a sum of Keplerian curves,

$$\mathcal{K}(t) = \sum_{j=1}^{N_{\text{pl}}} K_j \cdot [\cos(\nu_j(t) + \omega_j) + e_j \cos(\omega_j)], \quad (3)$$

where each planet  $j$  has a period  $P_j$ , semi-amplitude  $K_j$ , eccentricity  $e_j$ , longitude of periastron  $\omega_j$ , time of periastron passage  $T_{0,j}$  and true anomaly  $\nu_j$ . Instrumental zero-points  $\gamma_{0,\text{INS}}$ , long-term trends  $\dot{\gamma}$ , and (optionally) linear correlations with stellar activity indices  $C_{\mathcal{A},\text{INS}} \cdot \mathcal{A}_{i,\text{INS}}$  (with  $\mathcal{A}_{i,\text{INS}}$  denoting the measured activity index and  $C_{\mathcal{A},\text{INS}}$  the coefficient) are included additively into Eq. 3. Two orbital angles remain unconstrained by RVs alone, the inclination  $i_j$  (tilt with respect to the plane of sky) and the longitude of ascending node  $\Omega_j$  (plane-of-sky orientation). Consequently, RVs measure only the minimum mass  $M_{\text{pl},j} \sin i_j$  via the mass function

$$\frac{P_j K_j^3 \sqrt{(1 - e_j^2)^3}}{2\pi G} = \frac{(M_{\text{pl},j} \cdot \sin i_j)^3}{(M_{\text{pl},j} + M_\star)^2}. \quad (4)$$

### 2.3. Astrometric model (Hipparcos-*Gaia* differencing with IAD+GOST)

We adopted the astrometric differencing approach of Feng et al. (2019, 2023, 2024a). Rather than relying only on catalogue-level proper motion differences, we (i) fitted the HIPPARCOS intermediate astrometric data (IAD, the along-scan measurements at  $\sim 1990$ – $1993$ ; van Leeuwen 2007); and (ii) propagated and projected our model at the *Gaia* reference epoch using scan angles from the *Gaia* observation forecast tool (GOST; ESA/DPAC 2016a,b). This IAD+GOST approach preserves the HIPPARCOS epoch information and properly matches *Gaia*'s along-scan sensitivity, avoiding the information loss that can occur when collapsing to catalogue-level proper motion anomalies.

We propagated a five-parameter astrometric model between HIPPARCOS and *Gaia* epochs ( $\Delta\alpha$ ,  $\Delta\delta$ ,  $\Delta\mu_\alpha$ ,  $\Delta\mu_\delta$ ,  $\Delta\varpi$ ), including perspective terms from catalogue RV and parallax. We added the star's 3D reflex motion due to the companion(s) and projected it onto the sky. Internally, we used Thiele-Innes constants to map Keplerian elements to sky-plane displacements (for a detailed description, see Xiao et al. 2024). For every HIPPARCOS scan,

we computed the predicted along-scan displacement from the model (barycentre + reflex) at the scan time and angle and evaluated a Gaussian likelihood using the IAD uncertainties plus an additive jitter term  $J_{\text{hipp}}$ . On the other hand, at the *Gaia* reference epoch, we projected the model into *Gaia*'s along-scan direction using the GOST angles and parallax factors and formed the position and proper-motion differences relative to the HIPPARCOS solution linearly propagated to the *Gaia* epoch. The astrometric likelihood corresponds to the product of the HIPPARCOS-IAD term and the *Gaia* difference term. We included per-catalogue offsets and small frame-rotation jitters.

After linear-space motion was removed, a companion induced a sky-plane acceleration  $g$  that left two signatures over the HIPPARCOS-*Gaia* epoch separation  $\Delta t$ ,

$$\Delta r \approx \frac{1}{2} g (\Delta t)^2, \quad \Delta \mu \approx g \Delta t, \quad (5)$$

so jointly modelling positional ( $\Delta r$ ) and proper-motion ( $\Delta \mu$ ) offsets is especially sensitive to long-period companions. Using the actual scan geometries (GOST) reduces susceptibility to scan-angle-dependent systematics (e.g., Holl et al. 2023). Then, in this framework, the GOST model corresponds to the geometric projection layer that converts the orbital model in sky coordinates into *Gaia*'s effective along-scan observable using GOST scan geometry, while the GDR2/3 model corresponds to the statistical likelihood layer that compares that predicted mean vector to the catalogue-level *Gaia* solution using the reported covariance matrix. Using multi-epoch *Gaia* astrometry (GDR2 and 3) can help us to differentiate between prograde and retrograde orbits, breaking the inclination degeneracy (Xiao et al. 2024).

### 2.4. Priors

Our prior parameters were purposely flat for most RV and astrometric parameters. For long-period giants, the empirical eccentricity distribution is broad (Kipping 2013; Stevenson et al. 2025), but to regularise poorly constrained cases and to avoid bias towards spuriously high  $e$  in low-SNR regimes, we used a truncated normal prior  $\sim \mathcal{N}(0, 0.3) \in [0, 1]$ , penalising extremely higher eccentricities, but allowing them if supported by the data (see Tuomi et al. 2013). RV jitters use a wide truncated normal centred at zero, with the scale set by the average precision of the instrument, at either  $\sigma = 5$  or  $10 \text{ m s}^{-1}$ . HIPPARCOS additive astrometric jitter  $J_{\text{hipp}} \sim \mathcal{N}(1, 3)$  and fractional *Gaia* jitter  $S_{\text{gaia}} \sim \mathcal{N}(1, 0.1)$  absorb modest under- or over-dispersions.

For systems with two planets, we re-parametrised inclinations as  $(I_1, I_2) \mapsto (I_0, I_\Delta)$ , with

$$I_1 = I_0 - I_\Delta, \quad I_2 = I_0 + I_\Delta. \quad (6)$$

We favoured quasi-coplanarity via  $I_\Delta \sim \mathcal{N}(0, 5.73^\circ)$ , which is consistent with multi-planet mutual inclination dispersion (Fabrycky & Winn 2009; Zhu et al. 2018; He et al. 2020), while allowing separated inclinations if supported by the data. The reference inclination  $I_0 \sim \mathcal{I}(0, 180^\circ)$  uses an isotropic prior, uniform in  $\cos I_0$  over  $[0, 1]$ .

## 3. Target selection and observations

Since its inception, CHEPS has targeted quiet, metal-rich FGK stars (Jenkins et al. 2008; Jenkins & Jordán 2011) with the goal of discovering giant planets (Jenkins et al. 2009, 2017). For the present study, we selected CHEPS stars that showed significant long-term RV curvature or acceleration in the 2009–2021 time

**Table 1.** Stellar parameters.

Parameter	HIP 8923	HIP 10090	HIP 21850	HIP 39330	HIP 98599
<sup>1</sup> Spectral type	G3V	K0	G8V	G5V	F7V
<sup>1</sup> $B - V$	0.638	0.766	0.773	0.655	0.556
<sup>1</sup> $V$	8.24	8.94	8.41	7.52	8.11
<sup>1</sup> $S_{MW}$	$0.157 \pm 0.004$	$0.139 \pm 0.004$	$0.135 \pm 0.004$	$0.201 \pm 0.005$	$0.142 \pm 0.004$
<sup>1</sup> $\log R'_{HK}$	-5.01	-5.16	-5.18	-4.80	-5.10
<sup>1</sup> $v \sin i$ (km s <sup>-1</sup> )	3.0	2.7	2.8	3.4	8.0
<sup>1</sup> RV	$-22.75 \pm 0.13$	$9.20 \pm 0.17$	$62.63 \pm 0.12$	$23.03 \pm 0.13$	$-14.78 \pm 0.13$
<sup>2</sup> Mass ( $M_{\star}$ )	$1.01^{+0.04}_{-0.04}$	$0.94^{+0.04}_{-0.04}$	<sup>(3)</sup> $0.98^{+0.12}_{-0.12}$	$0.96^{+0.04}_{-0.04}$	$1.19^{+0.04}_{-0.04}$
<sup>4</sup> Distance (pc)	$65.87 \pm 0.11$	$82.30 \pm 0.11$	$55.50 \pm 0.06$	$36.39 \pm 0.02$	$76.10 \pm 0.13$
<sup>5</sup> [Fe/H]	$0.42 \pm 0.05$	$0.47 \pm 0.04$	$0.43 \pm 0.04$	$0.16 \pm 0.05$	$-0.12 \pm 0.10$
<sup>5</sup> $T_{eff}$ (K)	$5980 \pm 51$	$5661 \pm 72$	$5680 \pm 56$	$5748 \pm 81$	$5978 \pm 300$
<sup>5</sup> Age (Gyr)	$1.73^{+1.14}_{-1.22}$	$4.97^{+2.87}_{-1.69}$	$3.55^{+2.48}_{-2.19}$	$6.57^{+3.00}_{-1.96}$	$5.23^{+3.12}_{-3.71}$
Time baseline (yr)	14.80	16.98	24.83	17.01	20.82

**Notes.** (1) Perryman et al. (1997); (2) Kordopatis et al. (2023), (3) Feng et al. (2022), (4) Gaia Collaboration (2023), (5) This work with SPECIES Soto & Jenkins (2018).

series and continued monitoring them through 2025, thereby extending individual baselines up to  $\sim 16$  years. In addition to new CHEPS observations, we assembled all available high-precision archival RVs for these stars from HARPS, CORALIE, UCLES, and HIRES. For this first batch of CHEPS systems, we selected inactive stars ( $\log R'_{HK} \leq -4.75$ ), with low  $S_{MW}$  values ( $S_{MW} \leq 0.201$ ) that were also slow rotators ( $v \sin i \leq 5$  km s<sup>-1</sup>). Furthermore, we considered targets with a total RV baseline over 14 years and more than 16 CORALIE measurements (see the full stellar parameters in Table 1).

Our RV sample combines high-precision spectra from the High Accuracy Radial Velocity Planet Searcher (HARPS; Pepe et al. 2000) on the ESO 3.6 m telescope at La Silla Observatory; CORALIE (Udry et al. 2000) on the 1.2 m Euler telescope at La Silla Observatory; University College London Echelle Spectrograph (UCLES; Diego et al. 1990) at the Anglo-Australian Telescope (AAT); and the High Resolution Echelle Spectrometer (HIRES; Vogt et al. 1994) at the Keck Observatory. The HARPS data were retrieved from the public HARPS RVBank (Trifonov 2019; Perdelwitz et al. 2024), whilst UCLES and HIRES archival velocities were gathered from published releases and institutional archives.

HARPS experienced a fibre upgrade (2 June 2015) and a warm-up (23 March 2020) post-COVID shutdown (Lo Curto et al. 2015). Therefore, we treated HARPS with three different offsets: H (pre-2015), H15 (2015–2020), and H20 (post-2020).

CORALIE underwent a major upgrade in 2014. The circular fibre link was replaced with octagonal fibres, and a Fabry-Pérot calibration unit was added (Rickman et al. 2019). We adopted three subsets consistent with CHEPS processing: COR07 (pre-upgrade), COR14T (post-upgrades, reduced with TERRA; Anglada-Escudé & Butler 2012), and COR14 (post-upgrades, reduced with the CORALIE DRS).

We used the HIPPARCOS IAD from the new 2007 reduction (Perryman et al. 1997; van Leeuwen 2007), obtaining the data through `htof` (Brandt 2021), and *Gaia* DR3 five-parameter solutions (Gaia Collaboration 2023). To project our orbital models into *Gaia*'s measurement geometry at the *Gaia* reference epoch, we queried GOST for scan angles. A summary table with the number of measurements per target can be found in Table C.1.

## 4. Analysis and results

Within the EMPEROR framework, joint astrometry is straightforward to use, and a step-by-step tutorial can be found in the online documentation<sup>1</sup>.

For each target, we examined the RVs with generalised Lomb-Scargle periodograms (GLS; Lomb 1976; Scargle 1982), as well as with correlograms, calculating the Pearson-correlation coefficients between the RVs and stellar activity indices. We then began to fit models with EMPEROR, first by testing the null hypothesis that comprises just a mean and white noise (hereinafter  $0\mathcal{K}$ ). After this, we incrementally added Keplerian signals (models dubbed  $1\mathcal{K}$ ,  $2\mathcal{K}$ , and so on) and compared the Bayesian evidence  $\ln \widehat{\mathcal{Z}}$  with the previous model; with a difference of  $\Delta \ln \widehat{\mathcal{Z}} \geq 5$ , we selected the new model. Each model was run seven times to ensure consistent results. The values we present for the model comparison and parameter estimation correspond to the run with the median evidence. The hyper-parameter selection for our runs was set to 20 temperatures, 256 walkers, 80 000 sweeps, and 1 step for a grand total of 409 600 000 samples. Ladder adaptation was made with a uniform swap acceptance rate kernel, with a rate  $\nu_0 = 1.0$  and a timescale  $\tau_0 = 100$ . We left the adaptation for 40 000 sweeps and then froze the ladder. This initial phase we considered as burn-in, so these samples were dropped before any statistical inferences were made, preserving detailed balance so that standard ergodicity theorems apply.

As a validation case, we first analysed HIP 21850, a well-studied system hosting two confirmed exoplanets. We took as references the parameter solutions of Wittenmyer et al. (2017b, RV-only) and Feng et al. (2022, joint RV+astrometry) (W17 and F22, respectively). A summary of planet signatures for all systems can be found in Table 2.

### 4.1. HIP 21850

The RVs of planet HD 30177 present a highly significant peak in the GLS periodogram at above the 99.9% false-alarm probability (FAP) line at 2629 d. The GLS of the full width at half-maximum (FWHM) has a marginally significant peak between the 90%

<sup>1</sup> <https://astroemperor.readthedocs.io/en/latest/tutorials/astrometry>

**Table 2.** Planet signature summary for the joint RV+astrometry fit, with Jupiter analogues in bold.

Planet	Period (days)	Mass ( $M_J$ )	a (AU)	e	I ( $^\circ$ )
<b>HIP 8923b</b>	5160 <sup>+150</sup> <sub>-240</sub>	9.98 <sup>+0.78</sup> <sub>-0.16</sub>	5.90 <sup>+0.10</sup> <sub>-0.22</sub>	0.011 <sup>+0.032</sup> <sub>-0.011</sub>	24.8 <sup>+1.2</sup> <sub>-3.9</sub>
<b>HIP 10090b</b>	2960 <sup>+120</sup> <sub>-100</sub>	3.87 <sup>+0.65</sup> <sub>-0.60</sub>	3.87 <sup>+0.19</sup> <sub>-0.11</sub>	0.115 <sup>+0.005</sup> <sub>-0.033</sub>	156.5 <sup>+1.8</sup> <sub>-2.2</sub>
HIP 10090c	321.8 <sup>+0.3</sup> <sub>-0.6</sub>	0.85 <sup>+0.03</sup> <sub>-0.12</sub>	0.90 <sup>+0.01</sup> <sub>-0.01</sub>	0.188 <sup>+0.043</sup> <sub>-0.048</sub>	153.8 <sup>+1.3</sup> <sub>-3.1</sub>
<b>HIP 21850b</b>	2539 <sup>+1</sup> <sub>-3</sub>	8.25 <sup>+1.05</sup> <sub>-0.85</sub>	3.49 <sup>+0.18</sup> <sub>-0.14</sub>	0.186 <sup>+0.002</sup> <sub>-0.004</sub>	65.5 <sup>+1.7</sup> <sub>-4.2</sub>
HIP 21850c	11320 <sup>+490</sup> <sub>-940</sub>	4.67 <sup>+0.44</sup> <sub>-0.43</sub>	9.90 <sup>+0.29</sup> <sub>-0.62</sub>	0.210 <sup>+0.010</sup> <sub>-0.020</sub>	72.7 <sup>+17.8</sup> <sub>-5.8</sub>
<b>HIP 39330b</b>	4650 <sup>+210</sup> <sub>-250</sub>	1.67 <sup>+0.19</sup> <sub>-0.08</sub>	5.05 <sup>+0.23</sup> <sub>-0.17</sub>	0.078 <sup>+0.053</sup> <sub>-0.078</sub>	55.0 <sup>+0.6</sup> <sub>-3.9</sub>
<b>HIP 98599b</b>	2656 <sup>+40</sup> <sub>-16</sub>	6.85 <sup>+0.10</sup> <sub>-0.22</sub>	3.96 <sup>+0.07</sup> <sub>-0.01</sub>	0.169 <sup>+0.002</sup> <sub>-0.055</sub>	29.7 <sup>+6.9</sup> <sub>-6.2</sub>

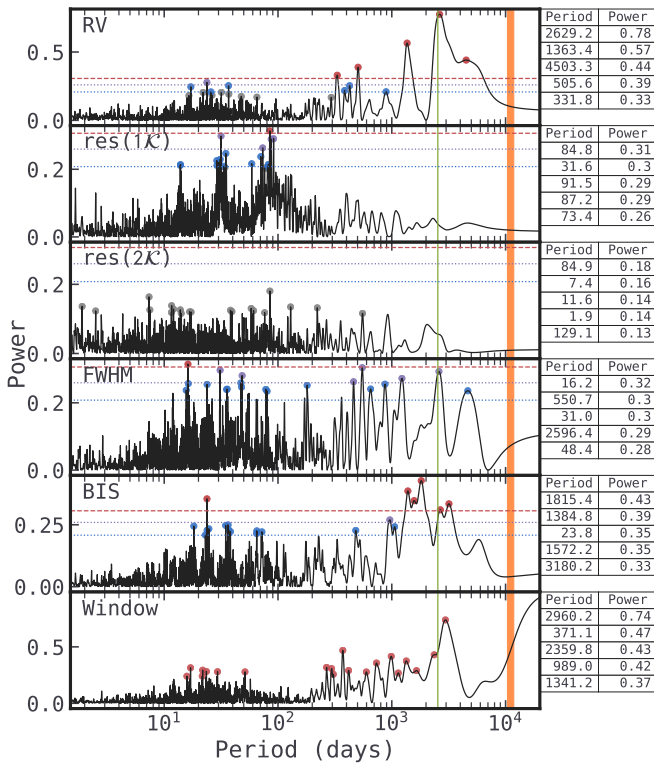


**Fig. 1.** HIP 21850 periodograms. Shown from top to bottom: RVs, model residuals, FWHM, BIS, and the window function. The FAP lines are included for 0.1, 1, and 10% and are plotted as dashed red, dotted purple, and dotted blue lines, respectively. The circles show the periods with the greatest power, coloured by FAP region. The coloured regions correspond to  $P_1 = 2539^{+0.8}_{-3.1}$  d (green) and  $P_2 = 11320^{+490}_{-940}$  d (orange).

and 99.0% FAP lines at 2596 d (see Fig. 1), while the bisector inverse slope (BIS) presents a highly significant peak at 2671 d. On the other hand, the correlogram reveals weak to moderate correlations ( $|\rho| \in [0.20, 0.60]$ ) between RVs and indices:  $\rho_{RV,FW} = -0.31$  for FWHM and  $\rho_{RV,BIS} = 0.45$  for BIS (see Fig. 2).

With the EMPEROR framework, we started by analysing RVs alone. The single-Keplerian solution ( $1\mathcal{K}$ ) finds an orbital period of  $P_1 = 2534^{+22}_{-11}$  d, and adding a second Keplerian ( $2\mathcal{K}$ ) yields periods  $P_1 = 2539.8^{+4.1}_{-4.7}$  d and  $P_2 = 15900^{+2500}_{-4800}$  d. The model comparison is decisive for the  $2\mathcal{K}$  model, as the Bayes factor (BF)  $\ln \hat{\mathcal{Z}} = 102.4$  strongly favours it, with a Bayesian evidence of  $\ln \hat{\mathcal{Z}}_{2\mathcal{K}} = -389.5 \pm 0.3$  over the  $1\mathcal{K}$  model's

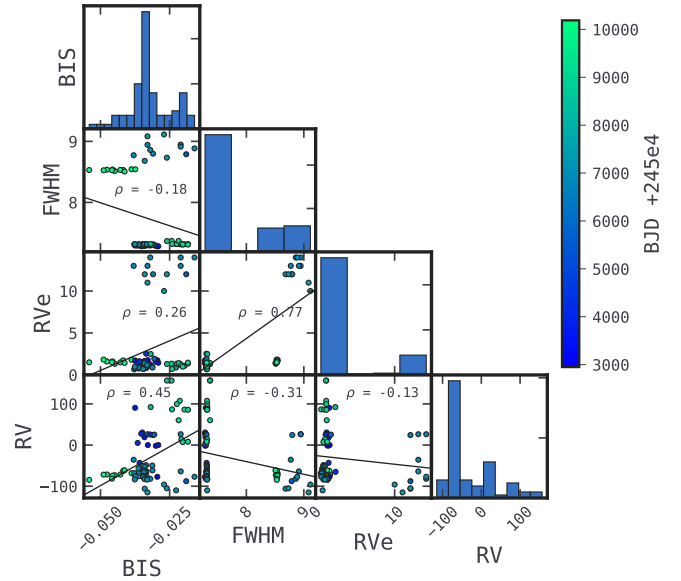


**Fig. 2.** HIP 21850 correlogram. Each panel displays the pairwise relation between RVs, FWHM, CCF BIS, and Rve. The Pearson correlation coefficient is denoted by  $\rho$ , and the linear trend is shown as a black line.

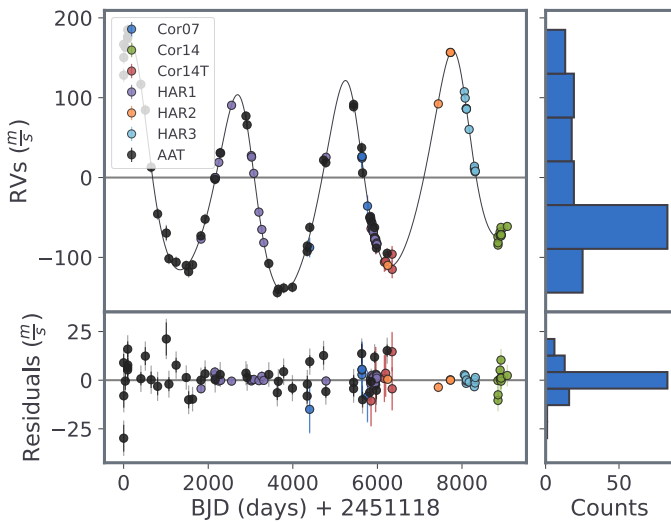
$\ln \hat{\mathcal{Z}}_{1\mathcal{K}} = -491.9 \pm 0.2$ . Each planet has minimum mass and semi-major axis estimates of  $m \sin i_1 = 8.2^{+0.1}_{-0.5} M_J$ ,  $m \sin i_2 = 6.6^{+1.4}_{-2.5} M_J$ ,  $a_1 = 3.65^{+0.02}_{-0.11}$ , and  $a_2 = 12.5^{+1.4}_{-2.7}$ .

The preference is the same for EMPEROR with RV+astrometry,  $\ln \hat{\mathcal{Z}}_{2\mathcal{K}} = -713.4 \pm 0.3$  over  $\ln \hat{\mathcal{Z}}_{1\mathcal{K}} = -817.5 \pm 0.3$ , with a BF of  $\Delta \ln \hat{\mathcal{Z}} = 104.10$  (we extensively discuss the BF differences with the addition of astrometry in Sect. 5.1). This time, we find  $P_1 = 2539^{+1}_{-3}$  d and  $P_2 = 11320^{+490}_{-940}$  d, with true masses and semi-major axes  $M_1 = 8.25^{+1.05}_{-0.85} M_J$ ,  $M_2 = 4.67^{+0.44}_{-0.43} M_J$ ,  $a_1 = 3.49^{+0.18}_{-0.14}$ , and  $a_2 = 9.90^{+0.29}_{-0.62}$  (see Table 3).

The inclusion of astrometry significantly helps us to constrain the second period,  $P_2 = 15900^{+2500}_{-4800} \rightarrow 11320^{+490}_{-940}$  d, while determining the true masses. The posteriors for the  $2\mathcal{K}$  RV-only model reveal that  $P_2$  sits uncomfortably in a posterior with a flattened top between  $\sim 9000$ – $17000$  d, as attested by the loose uncertainties. The RV+astrometry posteriors round significantly, still with a flattened top around  $11000$ – $12000$  d, which adds a clear upper boundary on the solution. Our solution remains fairly similar to those of W17 and F22, considering that with the addition of the CHEPS RV data, we extended the baseline from  $\sim 6000$  d to  $9070$  d. The RV part of the joint-model fit is shown in Fig. 3. The

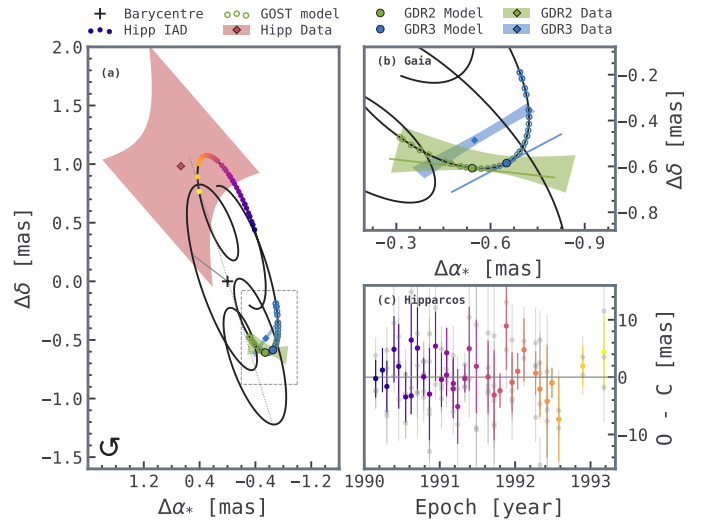
**Table 3.** HIP 21850 joint RV+astrometry parameter estimates.

Parameter	Prior	Wittenmyer et al. (2017b)	Feng et al. (2022)	This work
$P_1$ (days)	$\sim\mathcal{U}(1, 20\,000)$	$2524.4\pm 9.8$	$2514.5^{+5.2}_{-4.3}$	$2539^{+1}_{-3}$
$K_1$ ( $\text{m s}^{-1}$ )	$\sim\mathcal{U}(0+, 200)$	$126.3\pm 1.5$	$128.9^{+2.4}_{-2.2}$	$124.1^{+1.4}_{-1.0}$
$e_1$	$\sim\mathcal{N}(0, 0.3)$	$0.184\pm 0.012$	$0.207^{+0.012}_{-0.017}$	$0.186^{+0.002}_{-0.004}$
$I_1$ $^\circ$	$\sim\mathcal{I}(0, 180)$	–	$85.39^{+14.35}_{-18.74}$	$65.5^{+1.7}_{-4.2}$
$a_1$ AU	–	$3.58\pm 0.01$	$3.60^{+0.14}_{-0.15}$	$3.49^{+0.18}_{-0.14}$
$M_{p1}$ $M_J$	–	–	$8.40^{+1.24}_{-0.49}$	$8.25^{+1.05}_{-0.85}$
$P_2$ (days)	$\sim\mathcal{U}(1, 20\,000)$	$11\,613\pm 1837$	$12\,085^{+583}_{-441}$	$11\,320^{+490}_{-940}$
$K_2$ ( $\text{m s}^{-1}$ )	$\sim\mathcal{U}(0+, 200)$	$70.80\pm 29.50$	$54.47^{+5.17}_{-3.99}$	$41.03^{+1.60}_{-2.93}$
$e_2$	$\sim\mathcal{N}(0, 0.3)$	$0.22\pm 0.14$	$0.04^{+0.01}_{-0.01}$	$0.21^{+0.01}_{-0.02}$
$I_2$ $^\circ$	$\sim\mathcal{I}(0, 180)$	–	$98.02^{+16.03}_{-24.24}$	$72.7^{+17.8}_{-5.8}$
$a_2$ AU	–	$9.890\pm 1.040$	$10.26^{+0.55}_{-0.48}$	$9.90^{+0.29}_{-0.62}$
$M_{p2}$ $M_J$	–	–	$6.15^{+1.31}_{-0.34}$	$4.67^{+0.44}_{-0.43}$

**Fig. 3.** HIP 21850 RVs as circles coloured per instrument with the  $2\mathcal{K}$  model imposed as a black line. At the bottom, we plot the RV residuals, and in the right corner of each plot, we show RV distribution histograms.

astrometry is shown in Fig. 4. We further discuss the parameter estimates in Sect. 5.2.

For consistency, we again ran the RV residuals through the GLS: the RV field was flattened, with a single marginally significant peak at 90% in the FAP line at 91.1 d. Similarly, the residual correlogram was flat, with  $\rho_{RV,FW}=0.01$  and  $\rho_{RV,BIS}=-0.07$ . The flat residual periodogram and correlogram, the strong Bayesian preference, and the internal consistency of the  $P_1$  solution are good indicators for a planetary companion: if stellar activity were the origin of the main RV peaks, we would expect coherent residual power and/or correlations. Furthermore, all RV signals we discussed have larger amplitudes than are expected to be produced by stellar activity for these stars (up to a few  $\text{m s}^{-1}$ ; Makarov et al. 2009; Meunier et al. 2010). We further discuss the stellar activity and modelling with GPs with the EMPEROR framework in Peña R & Jenkins (2026).

**Fig. 4.** HIP 21850 best-fit astrometry for the  $2\mathcal{K}$  model. Panel a: best-fit astrometric orbit, the black cross is the system barycentre, the grey line connects it to the periastron, and the grey dotted line joins ascending and descending nodes. Reference epochs are shown as diamonds with their position and proper motion uncertainty as hourglass-shaped shaded regions. Green to blue coloured rings show GOST data projected with the best-fit. Solid circles and slopes show the best-fit position and proper motion induced by the companion. Panel b: zoom-in for the *Gaia* and GOST model (grey rectangle in panel a). Panel c: residuals for the HIPPARCOS abscissa as solid grey circles, where multiple measurements per epoch have been binned and coloured by time.

Finally, is worth discussing that the window function, initially a plausible source for some GLS structure given the peaks at 2960 and 2360 d, is unlikely to shape this solution: for  $1\mathcal{K}$ , the fitted  $P_1 = 2539$  d signal sits between the two window function spikes and survives in between when moving onto  $2\mathcal{K}$ , and even when astrometry is included in the fit.

#### 4.2. HIP 8923

The planet HIP 8923 is also known as HD 11731. The GLS periodogram (see Fig. A.1) shows three highly significant peaks

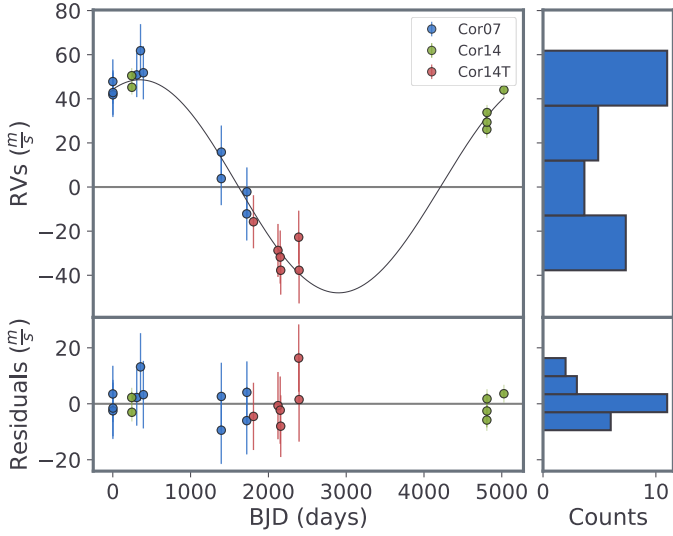


**Fig. 5.** HIP 8923 RVs phase-folded at  $P = 5160^{+150}_{-240}$  d as circles coloured per instrument with the  $1\mathcal{K}$  model imposed as a black line. At the bottom, we plot the RV residuals, and in the right of each plot, we show RV distribution histograms.

(>99.9% FAP line) in the RVs, at 5020 d and 314 d, which correspond to the yearly alias between 5020 d and 337 d in the window function, and at 29.7 d (the moon cycle), which is also present in the window function. The correlogram, on the other hand, shows a strong correlation (here defined as  $|\rho| \in [0.60, 0.80]$ ) in  $\rho_{RV,FW} = -0.63$ . This correlation might be an artefact due to the uncertainty difference between datasets, since there is a very strong correlation ( $\rho \in [0.80, 1]$ ) between the RV uncertainty and the FWHM  $\rho_{RVe,FW} = 0.97$ .

Our RV-only search yielded a single planet with an orbital period  $P_1 = 5120^{+460}_{-260}$  d, with evidence  $\ln \widehat{\mathcal{Z}}_{1\mathcal{K}} = -87.64 \pm 0.11$ , and a BF of  $\Delta \ln \widehat{\mathcal{Z}} = 16.77$  over the white-noise-only model  $\ln \widehat{\mathcal{Z}}_{0\mathcal{K}} = -104.41 \pm 0.09$ . By adding the astrometry data, we found  $P_1 = 5160^{+150}_{-240}$  d, which is consistent with the RV-only model. In this scenario, the evidence is  $\ln \widehat{\mathcal{Z}}_{1\mathcal{K}} = -297.97 \pm 0.19$ , with a  $\Delta \ln \widehat{\mathcal{Z}} = 75.35$  over the  $0\mathcal{K}$  model  $\ln \widehat{\mathcal{Z}}_{0\mathcal{K}} = -373.32 \pm 0.23$ .

This case strongly demonstrates the value of astrometry when only a part of a long-period orbit is sampled by RVs (see Fig. 5). The relative BF between  $0\mathcal{K}$  and  $1\mathcal{K}$  increases significantly when astrometry is added,  $\Delta \ln \widehat{\mathcal{Z}} = 16.77 \rightarrow 75.35$ . Furthermore, the inclusion of the astrometric data shrank the period uncertainty almost by half  $P_1 = 5120^{+460}_{-260} \mapsto 5160^{+150}_{-240}$  d, where the relative uncertainty corresponds to 13.97%, and 7.57%, respectively. Similarly, the minimum mass  $m \sin i = 4.30^{+0.07}_{-0.75} M_J$  becomes an absolute mass of  $M_1 = 9.98^{+0.78}_{-0.16} M_J$ , and semi-major axis  $a_1 = 5.89^{+0.30}_{-0.26} \mapsto 5.90^{+0.10}_{-0.22}$ . The complete astrometric fit can be seen Fig. 6.

Finally, we investigated the peak that appears in the window function at 4818 d. Even though it is ranked 12th in height, we analysed the residuals of the model: the GLS leaves no significant peaks above the 90% FAP line, which is a strong argument that the 5000-day power is well explained by the orbit rather than harmonics or aliases. On the other hand, the residual correlogram shows  $\rho_{res,FW} = 0.28$ , a significant shift from the initial  $\rho_{RV,FW} = -0.63$ . Even though this correlation is most likely an artefact due RV uncertainties between datasets, the strong anti-correlation disappears when the Keplerian is removed, which

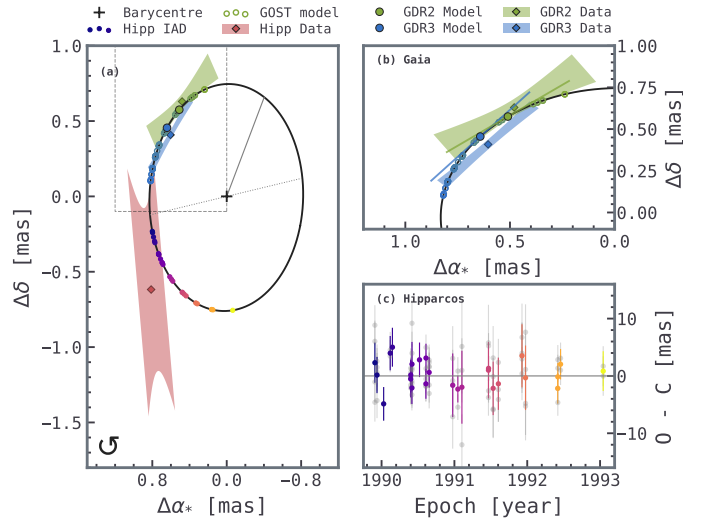


**Fig. 6.** HIP 8923 best fit for the  $1\mathcal{K}$  model. Panel a: best-fit astrometric orbit, the black cross is the system barycentre, the grey line connects it to the periapsis, and the grey dotted line joins ascending and descending nodes. Reference epochs are shown as diamonds with their position and proper motion uncertainty as hourglass-shaped shaded regions. Green to blue coloured rings show GOST data projected with the best-fit. Solid circles and slopes show the best-fit position and proper motion induced by the companion. Panel b: zoom-in for the *Gaia* and GOST model (grey rectangle in panel a). Panel c: residuals for the HIPPARCOS abscissa as solid grey circles, where multiple measurements per epoch have been binned and coloured by time.

is consistent with the planet driving most of the long-term RV variation, and does not indicate stellar activity. We also note that the yearly alias producing the second highest peak in the RVs at 314 d completely disappears in the residuals.

#### 4.3. HIP 10090

For HIP 10090, also known as HD 13350, our GLS periodogram reveals a dominant highly significant peak at 2892 d, another at 324 d, and a family of peaks around 25–32 d, corresponding to the lunar cycle. The stellar activity indices show no peaks above the 90% FAP line, and the window function shows peaks at 364 and 29.7 d, corresponding to the yearly and monthly aliases. The correlogram shows no significant correlations with stellar activity ( $|\rho| < 0.2$ ).

With *EMPEROR*, the RV-only solution settles at  $2\mathcal{K}$  with periods  $P_1 = 2980^{+140}_{-100}$  d and  $P_2 = 321.3^{+0.5}_{-0.4}$  d, with evidence  $\ln \widehat{\mathcal{Z}}_{2\mathcal{K}} = -203.84 \pm 0.18$ , and a BF of 10.92 over the  $\ln \widehat{\mathcal{Z}}_{1\mathcal{K}}$ . The runs including astrometry data settle at  $2\mathcal{K}$  as well, with  $P_1 = 2960^{+120}_{-100}$  d and  $P_2 = 321.8^{+0.3}_{-0.6}$  d (see Fig. 7), consistent with the RV-only solution. This run has  $\ln \widehat{\mathcal{Z}}_{2\mathcal{K}} = -548.57 \pm 0.19$ , with a BF of 27.22 over  $\ln \widehat{\mathcal{Z}}_{1\mathcal{K}}$ . By analysing the residuals of this model, the GLS stays flat, without peaks over the 90% FAP line, while the correlations remain insignificant. Once again, astrometry drives to a precise mass estimation  $m \sin i_1 = 1.53^{+0.12}_{-0.14} \mapsto M_1 = 3.87^{+0.60}_{-0.60} M_J$ , and  $m \sin i_2 = 0.39^{+0.02}_{-0.03} \mapsto M_2 = 0.85^{+0.03}_{-0.12} M_J$ .

The relatively high proper motion of HIPPARCOS (red ellipse in Fig. 8) makes this part of the model relatively uninformative compared to *Gaia* GDR2 and 3. We further discuss this point in Sect. 5.1.

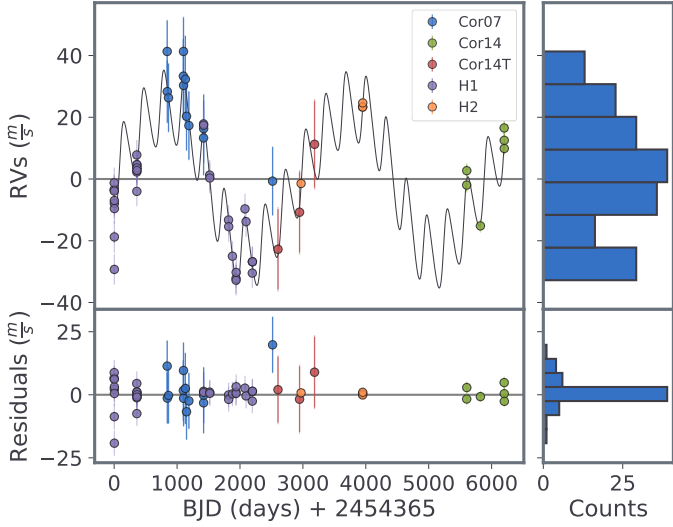


**Fig. 7.** HIP 10090 RVs as circles coloured per instrument with the  $2\mathcal{K}$  model imposed as a black line. At the bottom, we plot the RV residuals, and in the right of each plot, we show RV distribution histograms.

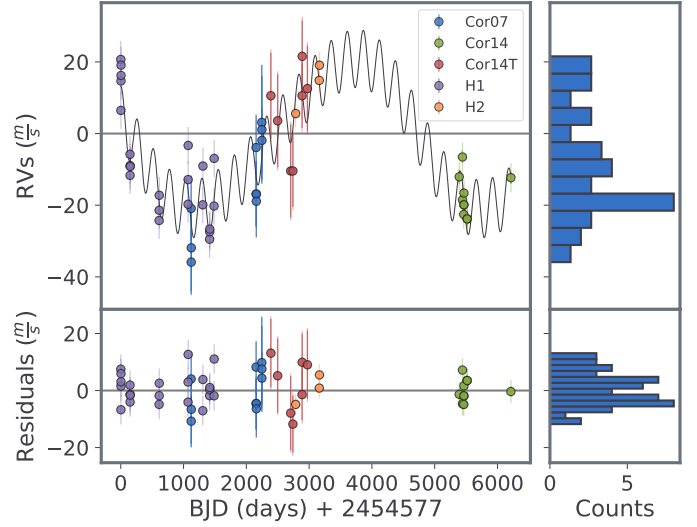


**Fig. 9.** HIP 39330 RVs as circles coloured per instrument with the  $2\mathcal{K}$  model imposed as a black line. At the bottom, we plot the RV residuals, and in the right corner of each plot, we show RV distribution histograms.

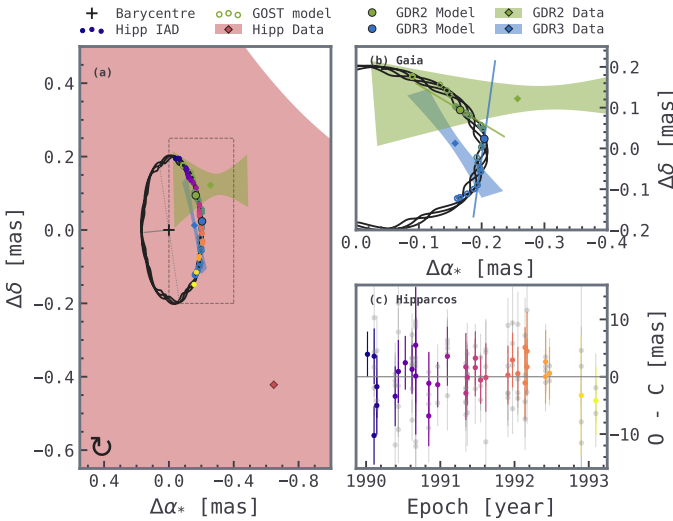


**Fig. 8.** HIP 10090 best fit for the  $2\mathcal{K}$  model. Panel a: best-fit astrometric orbit, the black cross is the system barycentre, the grey line connects it to the periapsis, and the grey dotted line joins ascending and descending nodes. Reference epochs are shown as diamonds with their position and proper motion uncertainty as hourglass-shaped shaded regions. Green to blue coloured rings show GOST data projected with the best-fit. Solid circles and slopes show the best-fit position and proper motion induced by the companion. Panel b: zoom-in for the *Gaia* and GOST model (grey rectangle in panel a). Panel c: residuals for the HIPPARCOS abscissa as solid grey circles, where multiple measurements per epoch have been binned and coloured by time.

#### 4.4. HIP 39330

For HIP 39330, also known as HD 66653, the GLS periodogram shows a single dominant peak in the RVs (see Fig. A.4) at 4547 d. The FWHM periodogram has significant peaks at 17.9 d and 29.0 d, the latter corresponding to the moon cycle. The correlogram does not reveal significant correlations ( $|\rho| < 0.2$ ) between RVs and stellar activity (see Fig. B.4).

The RV-only solution settles at  $1\mathcal{K}$  with  $P_1 = 4710_{-150}^{+20}$  d, with  $\ln \widehat{\mathcal{Z}}_{1\mathcal{K}} = -202.41 \pm 0.14$ . The  $2\mathcal{K}$  solution presents higher

evidence  $\ln \widehat{\mathcal{Z}}_{2\mathcal{K}} = -198.48 \pm 0.17$ , but it does not comply with our previous requirement of  $\Delta \ln \widehat{\mathcal{Z}} = 3.93 < 5$ , finding orbital periods  $P_1 = 4640_{-200}^{+300}$  d, and  $P_2 = 257_{-75}^{+160}$  d.

The joint RV+astrometry analysis settles at  $2\mathcal{K}$  with  $\ln \widehat{\mathcal{Z}}_2 = -548.83 \pm 0.23$ , with a  $\Delta \ln \widehat{\mathcal{Z}} = 6.97$  over the  $1\mathcal{K}$ , with  $P_1 = 4596.9_{-154.0}^{+1.7}$  d, and  $P_2 = 257.1_{-1.4}^{+1.6}$  d (see Fig. 9). This system alone of our sample presents equally likely multiple peaks (see Fig. C.1). Our sampler, or any MCMC sampler, is characterised by not returning point estimates but full distributions for each parameter. Because we modelled an astrophysical phenomenon that in reality must have a single solution (and quantum orbits are not fashionable), we tried to identify a unique orbital configuration by treating the model uncertainty and handling it explicitly. Xiao et al. (2024) assessed that for astrometry data, two data points (i.e., HIPPARCOS and GDR3) are insufficient to determine the inclination, resulting in a bi-modal solution. A third point (from GDR2) resolved this conundrum for their orbital fitting. We diagnosed this phenomenon as the origin of our multimodality. For this particular system, GDR2 leaves little information (poor fit; see Fig. 10), leaving us with a bimodal solution.

Consequently, we tried to fit the modes separately and to quantify the odds. Instead of slicing the parameter space arbitrarily, we set a small normal prior on each possible inclination, with  $2\mathcal{K}_1 \sim \mathcal{N}(0.92, 0.3)$ , and  $2\mathcal{K}_2 \sim \mathcal{N}(2.29, 0.3)$ . As a result,  $\Delta \ln \widehat{\mathcal{Z}} = 0.15$  marginally favoured  $2\mathcal{K}_2$  (see the parameter summary for both models in Table D.4). We took the  $1\mathcal{K}$  model as our solution, and we further discuss this system in Sect. 5. We also took note of the third and second highest RV periodogram peaks at 403.8 d (which might correspond to the yearly alias with  $P_1$ ) and 57.7 d, which subsequently disappear in the residuals of  $1\mathcal{K}$  and  $2\mathcal{K}$ .

#### 4.5. HIP 98599

For HIP 98599 (or HD 189627), the GLS (see Fig. A.3) reveals a single peak dominating the RVs at 2695 d, and the FWHM GLS has highly significant peaks surrounding it, at 1819.0 d and 3953.9 d. The structure is similar to that of the FWHM in the

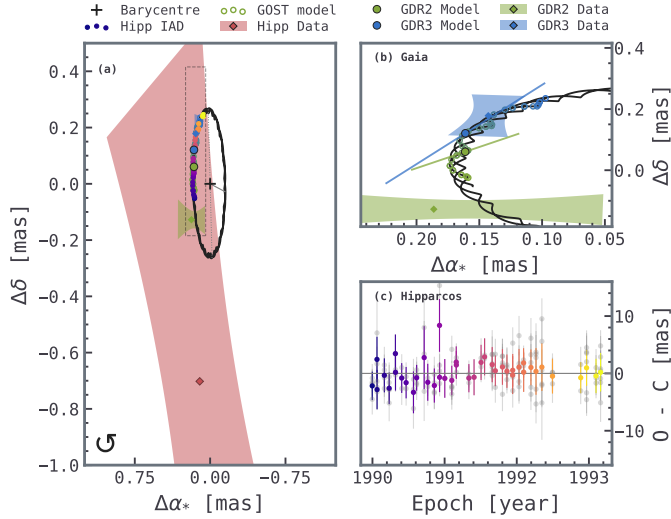


**Fig. 10.** HIP 39330 best fit for the  $2\mathcal{K}_1$  model. Panel a: best-fit astrometric orbit, the black cross is the system barycentre, the grey line connects it to the periapsis, and the grey dotted line joins ascending and descending nodes. Reference epochs are shown as diamonds with their position and proper motion uncertainty as hourglass-shaped shaded regions. Green to blue coloured rings show GOST data projected with the best-fit. Solid circles and slopes show the best-fit position and proper motion induced by the companion. Panel b: zoom-in for the *Gaia* and GOST model (grey rectangle in panel a). Panel c: residuals for the HIPPARCOS abscissa as solid grey circles, where multiple measurements per epoch have been binned and coloured by time.

BIS, but without significant power. The correlogram shows moderate to strong correlations ( $|\rho| \in [0.4, 0.8]$ ) between the RVs with FWHM and BIS:  $\rho_{RV,FW}=0.64$ ,  $\rho_{RV,BIS}=0.51$ . Similarly to HIP 8923, both correlations might be artefacts due to the uncertainty differences between datasets: the correlations between the RV uncertainty and indices are strong to very strong  $\rho_{RVe,FW}=0.96$ , and  $\rho_{RVe,BIS}=0.62$ . This is further supported by the correlations in the HARPS datasets alone,  $\rho_{RVHAR,FW}=-0.26$ , and  $\rho_{RVHAR,BIS}=-0.11$ , which shift from strongly positive to weakly negative.

The EMPEROR RV-only analysis settles at  $1\mathcal{K}$  with  $\ln \widehat{\mathcal{Z}}_{1\mathcal{K}} = -144.09 \pm 0.14$ , with  $\Delta \ln \widehat{\mathcal{Z}} = 47.50$  over the  $0\mathcal{K}$ , with  $P_1 = 2580^{+80}_{-90}$  d. The RV+astrometry analysis settles at  $1\mathcal{K}$  as well, with  $P_1 = 2656^{+40}_{-16}$  d (see Figs. 11 and 12), with  $\ln \widehat{\mathcal{Z}}_{1\mathcal{K}} = -543.01 \pm 0.20$ , and  $\Delta \ln \widehat{\mathcal{Z}} = 61.12$  over the  $0\mathcal{K}$  model, a BF difference of 13.62 with the RV-only model. This result also matches the main GLS peak in the RVs. Furthermore, examining the residuals of the GLS yields no periods above the 99.9% FAP line (see Fig. A.3), the most prominent ones ( $\geq 99.0\%$ ) at 7.2 d, 25.5 d and 155.9 d. The residual correlogram also flattens, with  $\rho_{RV,FW} = -0.09$ ,  $\rho_{RV,BIS}=0.17$ .

## 5. Discussion

The EMPEROR framework, with the addition of astrometric differencing modelling (Feng et al. 2019, 2021) introduced in Sect. 2.1, proves to be a useful tool for identifying and characterising cold giants. In our analysis of this first batch from the extended CHEPS (totalling an RV baseline of  $\sim 16$  yr), we validated our tool by refining orbital parameter estimates for HIP 21850 and fully characterised five new exoplanets: a warm Jupiter (HIP 10090c), four Jupiter analogues (HIP 8923b, HIP 10090b, HIP 98599b, and HIP 39330b), and a warm-Saturn candidate (HIP 39330c). They are summarised in Table 2. In this section, we quantify how the

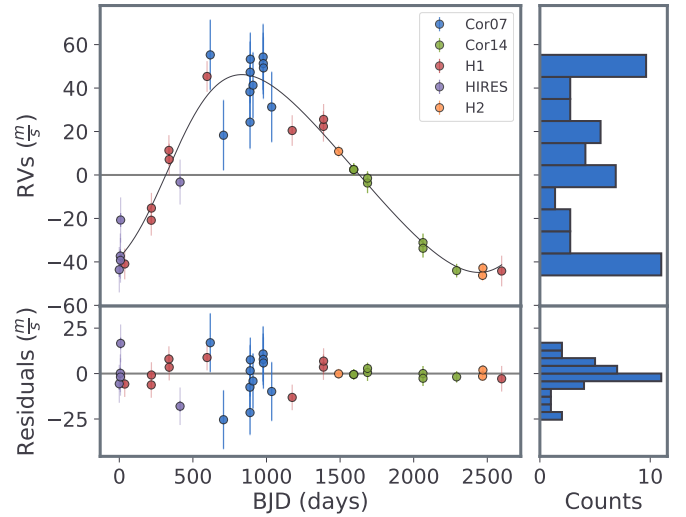


**Fig. 11.** HIP 98599 RVs phase-folded at  $P_1 = 2656^{+40}_{-16}$  d as circles coloured per instrument with the  $1\mathcal{K}$  model imposed as a black line. At the bottom, we plot the RV residuals, and in the right corner of each plot, we show RV distribution histograms.

inclusion of astrometry data boosts our confidence in the planetary solutions via Bayesian evidence and helps us to derive tighter uncertainties for the orbital parameters. Then, we discuss the multi-modality problem presented by HIP 39330, and we address how including small datasets affects our inference. Finally, we place the CHEPS planets of this study in context with the overall exoplanet population, and we highlight future opportunities.

### 5.1. Improved model evidence

Adding astrometry resulted in periods that were consistent with those found by RVs alone, and it also improved the Bayes factor between models. Defining this increase as  $\Delta \text{BF} = \Delta \ln \widehat{\mathcal{Z}}_{RV+AM} - \Delta \ln \widehat{\mathcal{Z}}_{RV}$ , we found a wide range of model comparison improvements. In HIP 8923, we have  $\Delta \text{BF} = 58.58$ , whereas in HIP 21850, we have  $\Delta \text{BF} = 1.70$ . To further analyse this increase, we briefly introduce two metrics for our data, a phase-coverage metric  $\Phi_c(P) \in [0, 1]$ , and a baseline-coverage metric  $\beta_c \in \mathbb{R}^+$ . For a given test period  $P$ , we mapped to phase each observation time  $t_i$ , with  $i = (0, \dots, n)$  for  $n$  observations as

$$\phi_i \equiv \left( \frac{t_i - t_0}{P} \right) \pmod{1}. \quad (7)$$

Then, we sorted the phases and computed the circular gap  $g_i$ ,

$$g_i = \begin{cases} \phi_{i+1} - \phi_i & \text{for } i = 1, \dots, n-1 \\ 1 - \phi_n + \phi_1 & \text{for } i = n \end{cases}. \quad (8)$$

Each  $g_i$  reveals the observational gap in phase. With  $\Phi_c \equiv \max(g_i)$ , we have a metric for phase incompleteness, where  $\Phi_c \rightarrow 0$  translates into a full period coverage (impossible for a finite sample), and  $\Phi_c \rightarrow 1$  to no phase coverage. We computed  $\Phi_c$  for a period grid  $[0, 20000]$  for each data type and system, obtaining a periodogram-like figure (see Fig. C.2), where peaks mark the periods that have the least coverage. Additionally, with the baseline coverage  $B(t)$  (how many orbital cycles the baseline spans), we calculated the baseline-coverage improvement ratio  $B_c$  as

$$B(t) = \frac{t_{\max} - t_{\min}}{P}, \quad B_c = \frac{B(t_{RV+AM})}{B(t_{RV})}. \quad (9)$$

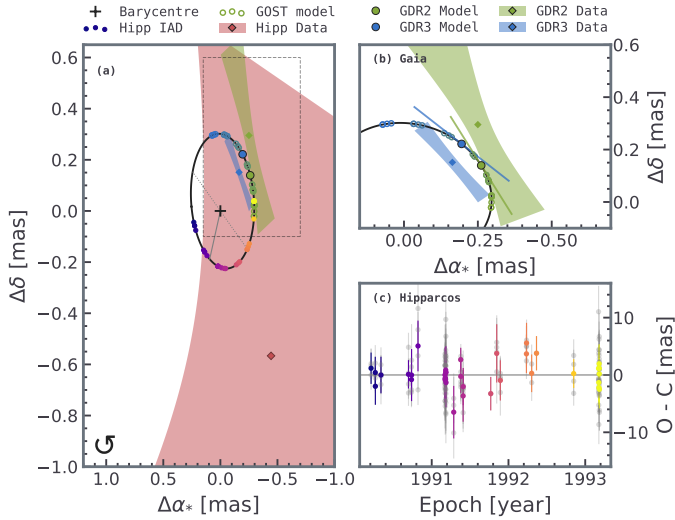


**Fig. 12.** HIP 98599 best fit for the  $1\mathcal{K}$  model. Panel a: best-fit astrometric orbit, the black cross is the system barycentre, the grey line connects it to the periapsis, and the grey dotted line joins ascending and descending nodes. Reference epochs are shown as diamonds with their position and proper motion uncertainty as hourglass-shaped shaded regions. Green to blue coloured rings show GOST data projected with the best-fit. Solid circles and slopes show the best-fit position and proper motion induced by the companion. Panel b: zoom-in for the *Gaia* and GOST model (grey rectangle in panel a). Panel c: residuals for the HIPPARCOS abscissa as solid grey circles, where multiple measurements per epoch have been binned and coloured by time.

We used these metrics because they capture the fraction of the orbital phase that is spanned by observations ( $\Phi_c$ ) and the extent to which astrometry extends the temporal baseline ( $B_c$ ) in an intuitive way.

For HIP 8923, we have  $\Delta\text{BF} = 58.58$ , a tremendous information jump by the inclusion of the astrometry data. This is easily explained: for our period of interest ( $P_1 \approx 5162$  d),  $\Phi_c$  decreases considerably with the addition of astrometry data, from  $\Phi_{c,\text{RV}} = 0.468$  to  $\Phi_{c,\text{RV+AM}} = 0.194$ . This can be seen by comparing the height ( $\Phi_c$ ) of the blue line (RV) against the purple line (RV+AM), across the green vertical bar ( $P_1 \approx 5162$  d) in Fig. C.2). A summary of comparative values can be found in Table 4. The evidence uncertainties are all  $\approx 0.2$ , and the  $\Delta\text{BF}$  uncertainty is  $\approx 0.3$ . The exact evidence uncertainties can be found in Sect. 4.

At the other extreme, HIP 21850 has the smallest  $\Delta\text{BF} = 1.70$ , which is well explained by  $\Phi_c$  barely increasing with astrometry  $\Delta\Phi_c = 0.016$  (in Fig. C.2, our period lies in a peak), and the lowest baseline-coverage ratio  $B_c = 1.687$ .

HIP 10090 has the second largest increase  $\Delta\text{BF} = 16.30$ . While not directly explained by coverage metrics, a secondary peak appears in the RV posteriors at 395 d, with  $\Delta\text{likelihood} \sim 6$  from the maximum, which is dispelled with astrometry. In contrast, while it has good coverage metrics, the addition of astrometry creates a multimodal solution for HIP 39330, penalising the overall model likelihood, with the second lowest  $\Delta\text{BF} = 3.04$ . The phase coverage provided by the astrometry in Fig. C.2 shows that our long period resides right in the middle of a red peak  $\Phi_{c,\text{AM}} = 0.723$ , meaning that astrometry does not provide good coverage at all. The short period (vertical orange line), while being almost completely covered  $\Phi_{c,\text{AM}} \sim 0$ , is almost imperceptible in the astrometry data (see the small wobble in Fig. 10). It is worth mentioning that the inclusion of astrometry,

**Table 4.** Improvement of BF and coverage metrics ( $\Phi_c$  for phase and  $B_c$  for baseline) with joint RV+astrometry over RV only.

Planet	Period (days)	$\Delta\text{BF}$	$\Delta\Phi_c$	$B_c$
HIP 8923b	$5160^{+150}_{-240}$	58.58	0.274	2.372
HIP 10090b	$2960^{+120}_{-100}$	16.30	0.062	2.068
HIP 21850c	$11\,320^{+490}_{-940}$	1.70	0.016	1.414
HIP 39330b	$4650^{+210}_{-250}$	3.04	0.108	2.064
HIP 98599b	$2656^{+40}_{-16}$	13.62	0.056	1.687

while mostly uninformative for the  $2\mathcal{K}$  model, does indeed help with the first signal. When we compare the BF increase between  $0\mathcal{K}$  and  $1\mathcal{K}$ , the increase is  $\Delta\text{BF} = 9.30$ .

## 5.2. Improved planet parameter estimates

Most of our systems present improved parameter estimates. For example, the mass determination helped us to secure HIP 10090c from an ambiguous Saturn  $m \sin i = 0.39^{+0.02}_{-0.03} M_J$  to a bona fide Jupiter-mass planet  $M = 0.85^{+0.03}_{-0.12} M_J$ . For HIP 21850, we have tighter period constraints  $P_1 = 2534^{+22}_{-11} \rightarrow 2539^{+1}_{-3}$  d, and for the second period  $P_2 = 15\,900^{+2500}_{-4800} \rightarrow 11\,320^{+490}_{-940}$  d, the uncertainties are reduced by almost an order of magnitude, as are the near-coplanar orbits  $\Delta I = 7.2^\circ$  for this system. For HIP 98599, the period uncertainty range is reduced by a third  $P_1 = 2580^{+80}_{-90} \rightarrow 2656^{+40}_{-16}$  d.

For HIP 39330, the situation is awkward and effectively leaves us with two astrometric solutions. This means that our data are genuinely insufficient for identifying a unique orbital configuration (see Fig. C.1), bifurcating the second orbital period into two distinct solutions,  $P_{2,1} \approx 255$  d and  $P_{2,2} \approx 260$  d, and leaving us unable to resolve the inclination degeneracy. We fitted each mode separately with normal priors on the inclination  $I_{1,1} \sim \mathcal{N}(0.92, 0.3)$ , and  $I_{1,2} \sim \mathcal{N}(2.29, 0.3)$  and quantified their odds, which are virtually equal. While there is enough evidence to confidently claim a second signal, we cannot confidently characterise it. Conservatively, we prefer adopting the simpler  $1\mathcal{K}$  model, until further astrometric data are available to break this degeneracy. The parameter summaries for each mode can be found in Table D.4.

## 5.3. Sufficient RV data

Our need to split RV datasets into subsets as small as  $N = 3$  (see Table C.1) raises the question whether the information obtained by so few points is worth the additional offset parameter. We examined HIP 10090 in detail, which is composed of a grand total of 57 RVs—12 COR07, three COR14T, six COR14, 32 H, and four H15 (datasets defined in Sect. 3). Out of these datasets, COR07, COR14T, and H15 do not provide additional baseline. Furthermore, their RV phase coverage is shared with other datasets. We compared the full RV phase incompleteness against the RVs without each of these sets (which we denote with the sub-indices  $-C07$ ,  $-C14T$ , and  $-H15$ ), obtaining for the long period  $P_1 = 2960^{+120}_{-100}$  the values  $\Phi_{c,\text{RV}} = 0.163$ ,  $\Phi_{c,-C07} = 0.213$ ,  $\Phi_{c,-C14T} = 0.163$ , and  $\Phi_{c,-H15} = 0.163$ , and for the short period  $\Phi_c = 0.136, 0.158, 0.136$ , and  $0.141$  for all combined datasets, and  $-COR07$ ,  $-COR14T$ , and  $-H15$ , respectively. With the exception of COR07 for the long period, none of these sets has a unique phase coverage, which is reflected in the phase-coverage metric, which remains at 0.163 when datasets are removed. Several interesting

**Table 5.** Summary of Bayes’ factors and coverage metrics.

Planet	$\Phi_{c,RV}$	$\ln \widehat{\mathcal{Z}} _{1\mathcal{K}}$	$\ln \widehat{\mathcal{Z}} _{2\mathcal{K}}$	$\Delta \ln \widehat{\mathcal{Z}}$
FULL	0.163	-562.79	-535.57	27.22
-COR07	0.213	-517.67	-490.01	27.65
-COR14T	0.163	-546.02	-534.14	11.88
-H15	0.163	-552.12	-525.43	26.69
-COR14T,H15	0.163	-535.35	-524.00	11.36

points arise when we examine the evidence (see Table 5). Out of these subsets, COR07 drives the most evidence, presenting the highest evidence gap with respect to the full RVs  $\sim 45$  for  $1\mathcal{K}$  and  $2\mathcal{K}$ . As expected, the solution loosens for the long period  $P_1 = 2920^{+180}_{-120}$  d, while remaining within the uncertainties below unity for  $P_2 = 321.38^{+0.69}_{-0.23}$  d. Nonetheless, this information does not contribute to the model comparison, with similar  $\Delta \ln \widehat{\mathcal{Z}}$  to the full RVs  $\Delta \ln \widehat{\mathcal{Z}} = 27.22 \approx 27.65$ . A similar phenomenon occurs for H15, but is driven by the high precision of the data instead of their quantity, where the model comparison stays similar ( $\Delta \ln \widehat{\mathcal{Z}} = 27.22$ ), with the long-period uncertainty increasing when removing H15  $P_1 = 3250^{+130}_{-230}$  d, and  $P_2 = 320.71^{+1.04}_{-0.04}$  d staying similarly constrained. On the other hand, and perhaps unexpectedly, the three measurements by COR14T, while contributing the least to the overall evidence of  $2\mathcal{K}$  with an almost marginal difference of 1.43 against the full RV, have a crucial role in the model comparison by decreasing the  $\Delta \ln \widehat{\mathcal{Z}}$  to 11.88 when removed (from 27.22). These three modest measurements have the peculiarity of overlapping with GOST data, driving the inclination and the astrometric offset posteriors to a tighter solution.

#### 5.4. Cold Jupiters and next steps

Our CHEPS analysis places four systems firmly in the Jupiter-analogue regime (masses of 0.3–13  $M_J$  on orbits of 3–7 AU) and provides a dynamical characterisation for each with modest eccentricities  $e \lesssim 0.19$  (see Table 2). Two of the planets, HIP 8923b and HIP 39330b, reside very close to Jupiter’s orbital scale ( $\sim 5$  AU), directly probing Solar System-like architectures. Furthermore, although we were unable to precisely constrain the inclination with our current data, HIP 39330c resides at  $\sim 1$  AU, making it a Jupiter-Earth-like system.

Of the more than 6000 exoplanets confirmed to date, only about one-third have true mass estimates (2223 according to Christiansen et al. 2025). Most of these come from transits (1567), so they predominantly sample short to intermediate orbital periods. Figure 13 situates these planets within the broader exoplanet census in the mass-distance plane. The CHEPS Jupiter analogues occupy the transitional swath in which the RV sensitivity declines with increasing  $a$  and direct imaging has focused beyond several AU. By combining decades of precise RV monitoring with HIPPARCOS-to-*Gaia* astrometry, we fill this demographic gap now with dynamical masses instead of minimum masses. This expands the well-vetted sample of true Jupiter analogues, improving constraints for population-level inferences and forward models of direct-imaging yields. Furthermore, the other two planets (HIP 10090c and HIP 39330c) occupy a much more sparsely populated region around  $\sim 1$  AU.

Beyond the characterisation of individual systems, joint RV+astrometry inference is rapidly becoming central to catalogue-level reliability. In practice, *Gaia* will turn many long-period RV

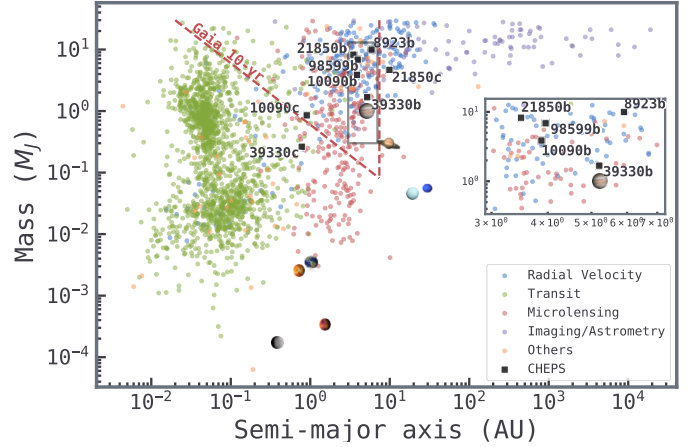


**Fig. 13.** True mass vs. semi-major axis of the confirmed exoplanet population from the NASA Exoplanet Archive (Christiansen et al. 2025), coloured by discovery method. The approximate sensitivity curve for GDR4 is shown as a dashed red line, assuming a Sun-like star at 20 pc and a  $3\sigma$  detection criterion. CHEPS targets from this study are shown as solid black squares. Solar System planets are shown as icons.

detections into directly testable hypotheses against *Gaia* astrometry, either reinforcing the planetary interpretation or exposing a difference that points to additional companions, alternative solutions, or underestimated systematics. This shift will also deliver a step change in mass completeness, moving a large fraction of long-period companions from minimum to true masses and thereby enabling cleaner demographics of cold giants and a more robust separation of planets from brown dwarfs and low-mass stellar companions. Our HIPPARCOS–*Gaia* differencing and joint-modelling approach already mirrors, in compressed form, the type of information *Gaia* DR4/DR5 will provide at scale through intermediate astrometry and non-single-star solutions, so the same modelling philosophy and vetting logic will carry over naturally. At the same time, *Gaia*-based candidate lists will inevitably include astrophysical contaminants (e.g. unresolved binaries), strengthening the case for joint, physically consistent modelling rather than naive catalogue ingestion.

These systems are ripe for targeted follow-up in the near future. Extended RV baselines will continue to refine long-period phase coverage, while upcoming astrometric surveys and data releases such as the *Rubin* Observatory Data Release 1 on May 2026 (LSST; Hambleton et al. 2023), *Gaia*’s DR4 in December 2026 (Brown 2024), the Roman Space Telescope in late 2026–2027 (Holler et al. 2025), or CHES (Ji et al. 2024) will sharpen accelerations and proper-motion anomalies, or even determine orbits on their own with intermediate data. The same RV+astrometry framework that proved decisive here is directly aligned with near-term and mid-term roadmaps for cold giant demographics and precursor target vetting for future missions. Therefore, we encourage the early adoption of available astrometric data in RV characterisation, providing full orbital parameters, as well as enhanced confidence in the modelled solutions, even when RVs alone might appear sufficient. In this context, CHEPS’ metal-rich, quiet FGK targets remain an efficient hunting ground for Solar System analogues that can anchor comparative planet studies across techniques. Building on CHEPS’ 16-year survey of  $\sim 240$  stars, already yielding cold giants, we are extending the observational baseline with continued monitoring. This will expand the sample of Jupiter analogues with true masses and full orbits, enabling a robust population-level census of Jupiter analogues.

## 6. Conclusions

We extended CHEPS by combining long-baseline RV data with absolute astrometry from the HIPPARCOS and *Gaia* missions to search for cold, wide-orbiting gas giants. Using the renewed EMPEROR framework enhanced with astrometric differencing, we have analysed five metal-rich FGK hosts and performed Bayesian model comparisons to identify planetary signals and quantify the improvement brought by astrometry.

The analysis confirmed the Jupiter-mass companions for HIP 21850, refined their orbital parameters with CHEPS data by extending the RV-baseline from  $\sim 16.4$  yr to  $\sim 24.6$  yr, and discovered four new Jupiter analogues: HIP 8923b, HIP 10090b, HIP 39330b, and HIP 98599b. We also identified a new warm Jupiter, HIP 10090c. True masses were derived through the astrometric inclination constraints, yielding estimates from  $\sim 1$  to  $\sim 10 M_J$  on orbits between  $\sim 1$  and  $\sim 7$  AU for the new planets (see Table 2). In one system (HIP 39330), the astrometric data led to a multi-modal solution for the second planet; adopting a simpler one planet model is prudent until additional data become available.

Incorporating astrometric data increased the BFs ranging from  $\sim 1.7$  to  $\sim 58.6$ , depending on phase coverage, baseline extension, and posterior multi-modality (see Table 4). The custom phase-coverage metrics we introduced showed that astrometry significantly reduces gaps in the orbital phase for cold giants and more than doubles the temporal baseline for some systems. This led to substantial reductions in the period and mass uncertainties, with an improvement of up to an order of magnitude for certain parameters. Even sparse astrometric measurements, when combined with RVs, can break the  $\sin I$  degeneracy and convert minimum masses into true masses.

The sufficiency test on HIP 10090 illustrated that not all RV subsets contribute equally. While some high-precision but phase-redundant datasets have a marginal effect, others with only a few observations can substantially affect the BF if they sample unique orbital phases. This underscores the need for strategically timed RV observations to complement astrometric data. The inability to constrain the inclination of HIP 39330c also highlights the current limitations of GDR2/GDR3 astrometry for certain orbital periods; *Gaia* DR4, *Rubin* DR1, and future missions will provide decisive improvements.

The CHEPS discoveries fill a demographic gap in the exoplanet census, occupying the transition region between RV-dominated detections and direct imaging (see Fig. 13). Establishing a sample of Jupiter analogues with dynamically measured masses will improve population statistics and refine predictions for direct-imaging yields. Continued RV monitoring and forthcoming astrometric releases will tighten the orbital constraints and possibly reveal additional companions. The RV+astrometry framework developed in this work is directly relevant to the nearby targets accessible to ELT coronagraphy and Roman Space Telescope; astrometry provides true masses, orbital geometry, and improved ephemerides that enable scheduling of direct detections and atmospheric characterisation of these cold worlds, which reside at the upper boundary of the planetary mass space.

By combining long-term RV monitoring with absolute astrometry, we demonstrated a powerful avenue for uncovering and characterising cold giant planets on Solar System-like orbits. The framework presented here positions CHEPS and similar surveys to exploit future data releases, paving the way towards a more complete understanding of planetary architectures around nearby stars.

## Data availability

Tables with RV measurements with CORALIE per target are available at the CDS via <https://cdsarc.cds.unistra.fr/viz-bin/cat/J/A+A/709/A213>. HARPS RVs (Perdelwitz et al. 2024) are available at <https://cdsarc.cds.unistra.fr/viz-bin/cat/J/A+A/683/A125>. UCLES/AAT RVs can be found in Wittenmyer et al. (2017a). HIRES RVs can be found in Butler et al. (2017). All RV and astrometry products used in this paper can be found in an EMPEROR-friendly format at <https://github.com/ReddTea/aa57940-25-data>.

*Acknowledgements.* All benchmarks were performed on a computer with an AMD Ryzen Threadripper 3990X 64-Core Processor with 128Gb of DDR4 3200MHz RAM, limiting the use to 24 physical cores and 24 threads. Type-setting was carried out in Overleaf (<https://www.overleaf.com>). PAPER and JSJ gratefully acknowledge support by FONDECYT grant 1240738 and from the ANID BASAL project FB210003. We also greatly appreciate the support from the CASSACA China-Chile Joint Research Fund through grant CCJRF2205. Part of this work was supported by the United States Fulbright Fellowship in partnership with the Fulbright Chile Commission, and ANID/Fondo ALMA 2024/No.31240039 “On the origin of Warm-Giant Planets”. We thank the anonymous referee for insightful suggestions that enhanced the quality of this manuscript.

## References

- Anglada-Escudé, G., & Butler, R. P. 2012, *ApJS*, 200, 15  
 Bonomo, A. S., Dumusque, X., Massa, A., et al. 2023, *A&A*, 677, A33  
 Brandt, T. D. 2021, *ApJS*, 254, 42  
 Brown, A. 2024, in *EAS2024, European Astronomical Society Annual Meeting*, 208  
 Bryan, M. L., Knutson, H. A., Lee, E. J., et al. 2019, *AJ*, 157, 52  
 Butler, R. P., Vogt, S. S., Laughlin, G., et al. 2017, *AJ*, 153, 208  
 Christiansen, J. L., McElroy, D. L., Harbut, M., et al. 2025, *PSJ*, 6, 186  
 Cumming, A., Butler, R. P., Marcy, G. W., et al. 2008, *PASP*, 120, 531  
 Diego, F., Charalambous, A., Fish, A. C., & Walker, D. D. 1990, *SPIE Conf. Ser.*, 1235, 562  
 Dressing, C., Ansdell, M., Crooke, J., et al. 2024, in *American Astronomical Society Meeting Abstracts*, 244, 210.04  
 Earl, D. J., & Deem, M. W. 2005, *PCCP*, 7, 3910  
 ESA/DPAC 2016a, *Gaia Observation Forecast Tool (GOST)*, <https://gaia.esac.esa.int/gost/>, accessed 2025-09-29  
 ESA/DPAC 2016b, *Gaia Observing Schedule Tool (GOST) – Software User Manual*, version 22.0.0; accessed 2025-09-29  
 Fabrycky, D. C., & Winn, J. N. 2009, *ApJ*, 696, 1230  
 Feng, F., Anglada-Escudé, G., Tuomi, M., et al. 2019, *MNRAS*, 490, 5002  
 Feng, F., Butler, R. P., Jones, H. R. A., et al. 2021, *MNRAS*, 507, 2856  
 Feng, F., Butler, R. P., Vogt, S. S., et al. 2022, *ApJS*, 262, 21  
 Feng, F., Butler, R. P., Vogt, S. S., Holden, B., & Rui, Y. 2023, *MNRAS*, 525, 607  
 Feng, F., Rui, Y., Xuan, Y., & Jones, H. 2024a, *ApJS*, 271, 50  
 Feng, F. B., Rui, Y. C., Du, Z. M., et al. 2024b, *AcASn*, 65, 34  
 Fischer, D. A., & Valenti, J. 2005, *ApJ*, 622, 1102  
 Fong, E., & Holmes, C. 2019, arXiv e-prints [arXiv:1905.08737]  
 Gaia Collaboration (Vallenari, A., et al.) 2023, *A&A*, 674, A1  
 Gan, T., Guo, K., Liu, B., et al. 2024, *ApJ*, 967, 74  
 Gelman, A., & Meng, X.-L. 1998, *Statist. Sci.*, 13, 163  
 Gonzalez, G. 1997, *MNRAS*, 285, 403  
 Hambleton, K. M., Bianco, F. B., Street, R., et al. 2023, *PASP*, 135, 105002  
 He, M. Y., Ford, E. B., Ragozzine, D., & Carrera, D. 2020, *AJ*, 160, 276  
 Holl, B., Fabricius, C., Portell, J., et al. 2023, *A&A*, 674, A25  
 Holler, B. J., Cosentino, R. G., Schultz, W. C., et al. 2025, arXiv e-prints [arXiv:2508.14412]  
 Ida, S., Lin, D. N. C., & Nagasawa, M. 2013, *ApJ*, 775, 42  
 Jenkins, J. S., & Jordán, A. 2011, in *Astronomical Society of the Pacific Conference Series*, 448, 16th Cambridge Workshop on Cool Stars, Stellar Systems, and the Sun, eds. C. Johns-Krull, M. K. Browning, & A. A. West, 991  
 Jenkins, J. S., Jones, H. R. A., Pavlenko, Y., et al. 2008, *A&A*, 485, 571  
 Jenkins, J. S., Jones, H. R. A., Goździewski, K., et al. 2009, *MNRAS*, 398, 911  
 Jenkins, J. S., Jones, H. R. A., Tuomi, M., et al. 2017, *MNRAS*, 466, 443  
 Ji, J., Li, H., Zhang, J., et al. 2024, *ChJSS*, 44, 193  
 Kervella, P., Arenou, F., & Thévenin, F. 2022, *A&A*, 657, A7  
 Kipping, D. M. 2013, *MNRAS*, 434, L51  
 Kordopatis, G., Schultheis, M., McMillan, P. J., et al. 2023, *A&A*, 669, A104

- Lammers, C., & Winn, J. N. 2026, *AJ*, 171, 18
- Lefèvre-Forján, E., & Mulders, G. D. 2025, *ApJ*, 988, 101
- Lo Curto, G., Pepe, F., Avila, G., et al. 2015, *Messenger*, 162, 9
- Lomb, N. R. 1976, *Ap&SS*, 39, 447
- Lothf, S., Izmailov, P., Benton, G., Goldblum, M., & Wilson, A. G. 2022, arXiv e-prints [arXiv:2202.11678]
- Makarov, V. V., Beichman, C. A., Catanzarite, J. H., et al. 2009, *ApJ*, 707, L73
- Meunier, N., Desort, M., & Lagrange, A.-M. 2010, *A&A*, 512, A39
- Mordasini, C., Alibert, Y., Benz, W., Klahr, H., & Henning, T. 2012, *A&A*, 541, A97
- Peña R, P. A., & Jenkins, J. S. 2026, *A&A*, 706, A323
- Pepe, F., Mayor, M., Delabre, B., et al. 2000, *SPIE Conf. Ser.*, 4008, 582
- Perdelwitz, V., Trifonov, T., Teklu, J. T., Sreenivas, K. R., & Tal-Or, L. 2024, *A&A*, 683, A125
- Perryman, M. A. C., Lindegren, L., Kovalevsky, J., et al. 1997, *A&A*, 323, L49
- Perryman, M., Hartman, J., Bakos, G. Á., & Lindegren, L. 2014, *ApJ*, 797, 14
- Rickman, E. L., Ségransan, D., Marmier, M., et al. 2019, *A&A*, 625, A71
- Robert, C. 2007, *The Bayesian Choice: From Decision-Theoretic Foundations to Computational Implementation*, Springer Texts in Statistics (Springer New York)
- Sagynbayeva, S., Abbas, A., Kane, S. R., et al. 2025, *AJ*, 170, 208
- Santos, N. C., Israelian, G., & Mayor, M. 2004, *A&A*, 415, 1153
- Scargle, J. D. 1982, *ApJ*, 263, 835
- Soto, M. G., & Jenkins, J. S. 2018, *A&A*, 615, A76
- Stevenson, A. T., Haswell, C. A., Faria, J. P., et al. 2025, *MNRAS*, 539, 727
- Trifonov, T. 2019, The Exo-Striker: Transit and radial velocity interactive fitting tool for orbital analysis and  $N$ -body simulations, Astrophysics Source Code Library [record ascl:1906.004]
- Tuomi, M., Anglada-Escudé, G., Gerlach, E., et al. 2013, *A&A*, 549, A48
- Udry, S., Mayor, M., Queloz, D., Naef, D., & Santos, N. 2000, in *From Extrasolar Planets to Cosmology: The VLT Opening Symposium*, eds. J. Bergeron, & A. Renzini, 571
- van Leeuwen, F. 2007, *A&A*, 474, 653
- Vogt, S. S., Allen, S. L., Bigelow, B. C., et al. 1994, *SPIE Conf. Ser.*, 2198, 362
- Vousden, W. D., Farr, W. M., & Mandel, I. 2016, *MNRAS*, 455, 1919
- Winn, J. N. 2018, in *Handbook of Exoplanets*, eds. H. J. Deeg, & J. A. Belmonte (Cambridge University Press), 195
- Wittenmyer, R. A., Horner, J., Mengel, M. W., et al. 2017a, *AJ*, 153, 167
- Wittenmyer, R. A., Jones, M. I., Horner, J., et al. 2017b, *AJ*, 154, 274
- Wittenmyer, R. A., Wang, S., Horner, J., et al. 2020, *MNRAS*, 492, 377
- Xiao, G.-Y., Feng, F., Shectman, S. A., et al. 2024, *MNRAS*, 534, 2858
- Xie, W., Lewis, P., Fan, Y., Kuo, L., & Chen, M.-H. 2011, *Syst. Biol.*, 60, 150
- Zhu, W., & Dong, S. 2021, *ARA&A*, 59, 291
- Zhu, W., Petrovich, C., Wu, Y., Dong, S., & Xie, J. 2018, *ApJ*, 860, 101

Appendix A: Periodograms

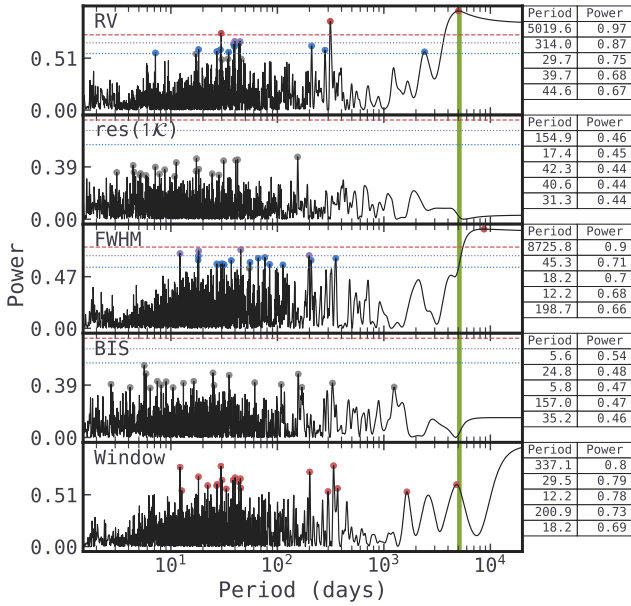


**Fig. A.1.** HIP 8923 periodograms. Shown from top to bottom: RVs, model residuals, FWHM, BIS, and window function. FAP lines for 0.1, 1, and 10%, in dashed red, dotted purple, and dotted blue, respectively. Circle markers show the periods with greatest power, coloured by FAP region. Green vertical region shows  $P_1 = 5160^{+150}_{-240}$  d. On the right side there is a table summary of the five highest powers.

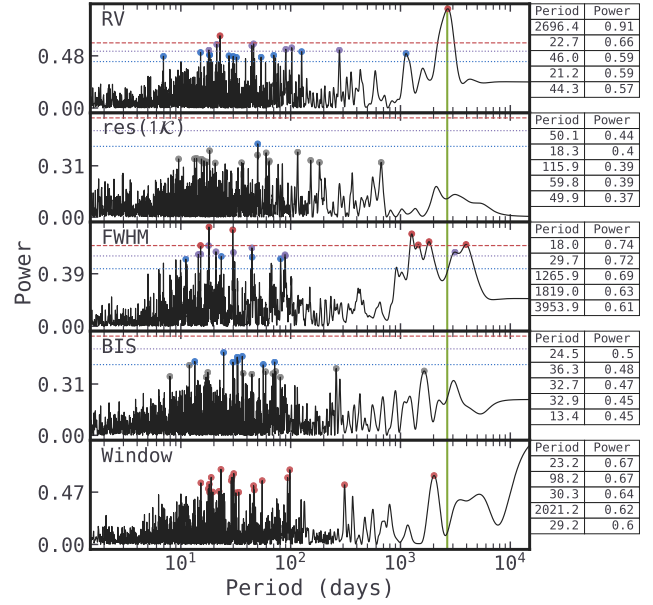


**Fig. A.2.** HIP 10090 periodograms. Shown from top to bottom: RVs, model residuals, FWHM, BIS, and window function. FAP lines for 0.1, 1, and 10%, in dashed red, dotted purple, and dotted blue, respectively. Circle markers show the periods with greatest power, coloured by FAP region. Green and orange vertical regions show  $P_1 = 2960^{+120}_{-100}$  d and  $P_2 = 321.82^{+0.32}_{-0.56}$  d, respectively. On the right side, a table summary with the highest powers.

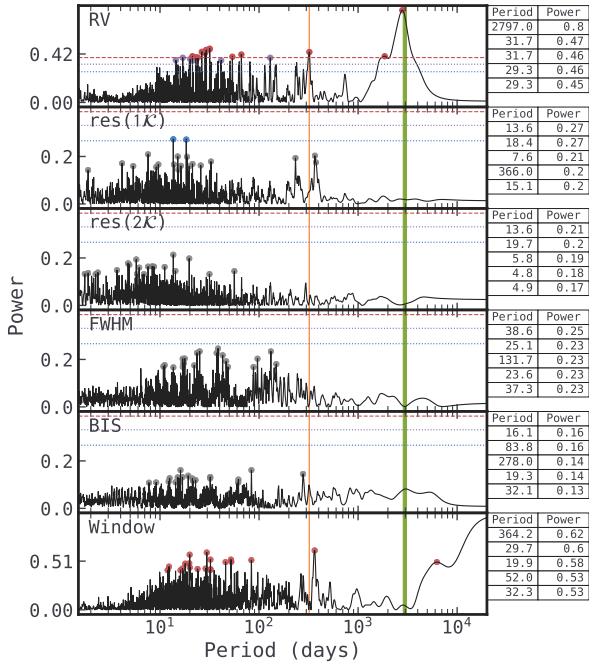


**Fig. A.3.** HIP 98599 periodograms. Shown from top to bottom: RVs, model residuals, FWHM, BIS, and window function. FAP lines for 0.1, 1, and 10%, in dashed red, dotted purple, and dotted blue, respectively. Circle markers show the periods with greatest power, coloured by FAP region. Green vertical region shows  $P_1 = 2656^{+40}_{-16}$  d. On the right side there is a table summary of the five highest powers.

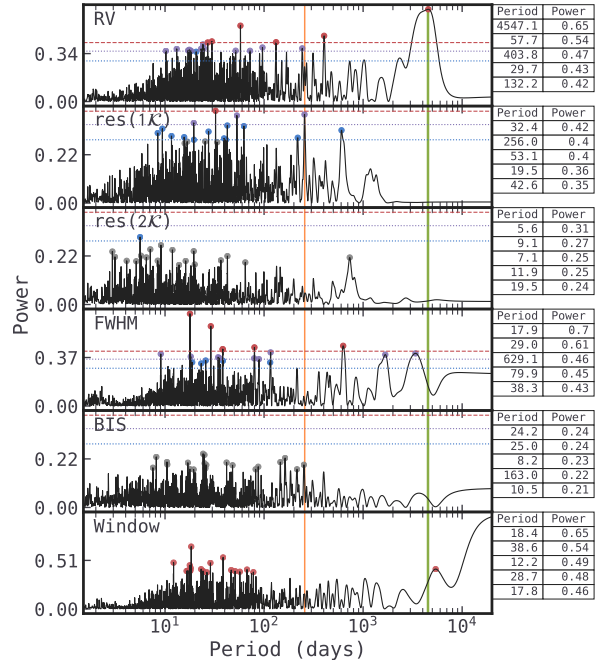


**Fig. A.4.** HIP 39330 periodograms. Shown from top to bottom: RVs, model residuals, FWHM, BIS, and window function. FAP lines for 0.1, 1, and 10%, in dashed red, dotted purple, and dotted blue, respectively. Circle markers show the periods with greatest power, coloured by FAP region. Green and orange vertical regions show  $P_1 = 4596.9^{+1.7}_{-154.0}$  d and  $P_2 = 257.1^{+1.6}_{-1.4}$  d, respectively. On the right side, a table summary with the highest powers.

Appendix B: Correlograms

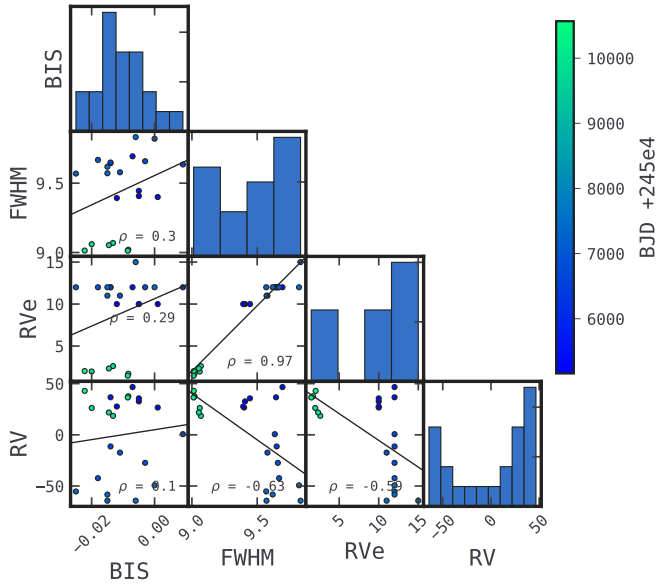


**Fig. B.1.** HIP 8923 correlogram. Each panel displays the pairwise relation between RVs, full-width half-maximum (FWHM), CCF bisector inverse slope (BIS), and formal RV uncertainty (RVe). Pearson correlation coefficient is denoted by  $\rho$ , with the linear trend as a black line.

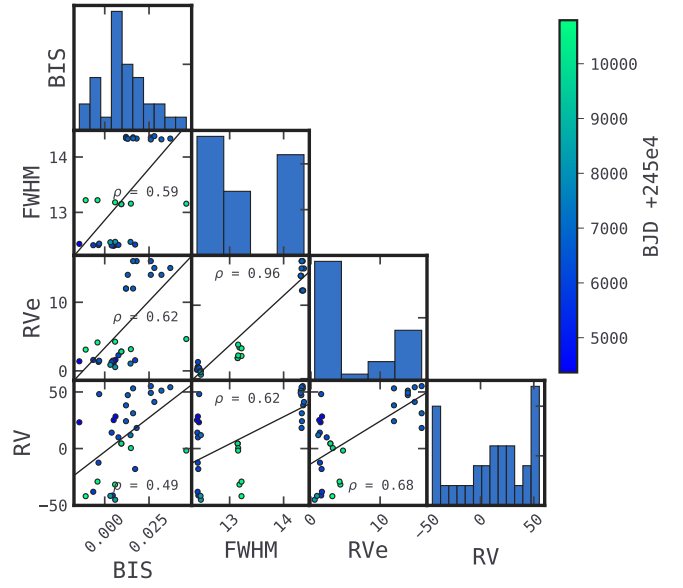


**Fig. B.2.** HIP 10090 correlogram. Each panel displays the pairwise relation between RVs, full-width half-maximum (FWHM), CCF bisector inverse slope (BIS), and formal RV uncertainty (RVe). Pearson correlation coefficient is denoted by  $\rho$ , with the linear trend as a black line.

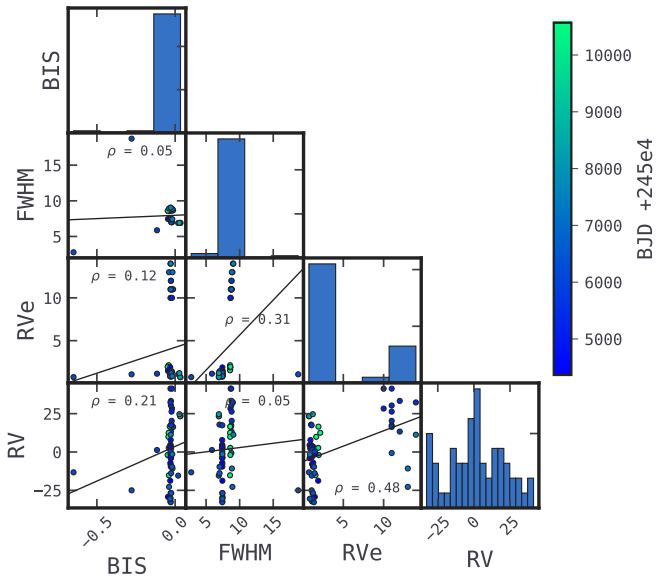


**Fig. B.3.** HIP 98599 correlogram. Each panel displays the pairwise relation between RVs, full-width half-maximum (FWHM), CCF bisector inverse slope (BIS), and formal RV uncertainty (RVe). Pearson correlation coefficient is denoted by  $\rho$ , with the linear trend as a black line.

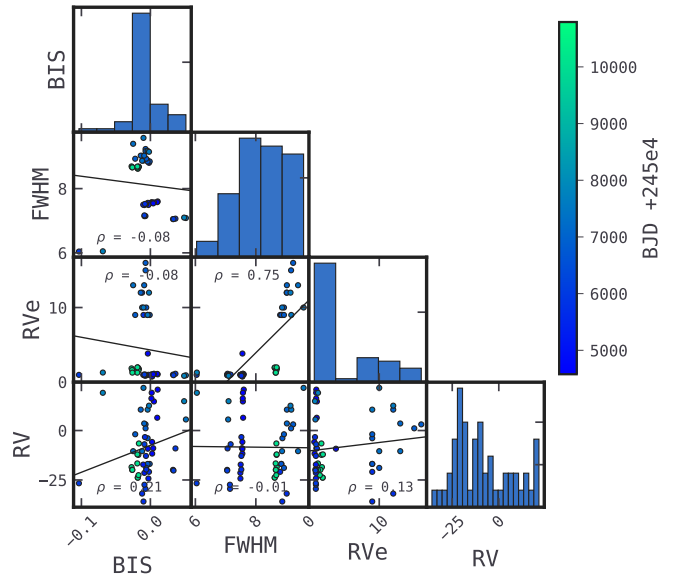


**Fig. B.4.** HIP 39330 correlogram. Each panel displays the pairwise relation between RVs, full-width half-maximum (FWHM), CCF bisector inverse slope (BIS), and formal RV uncertainty (RVe). Pearson correlation coefficient is denoted by  $\rho$ , with the linear trend as a black line.

Appendix C: Discussion

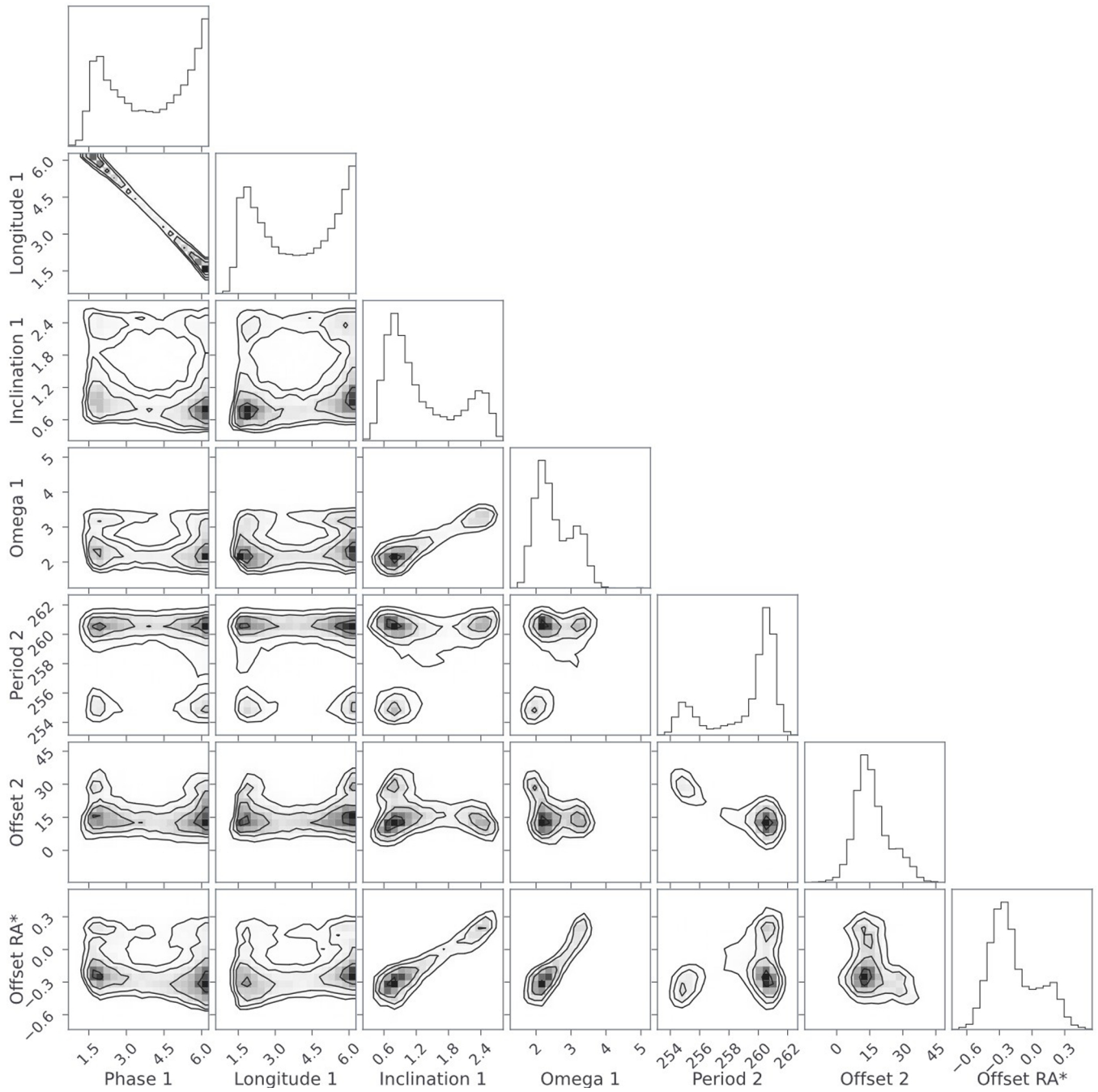
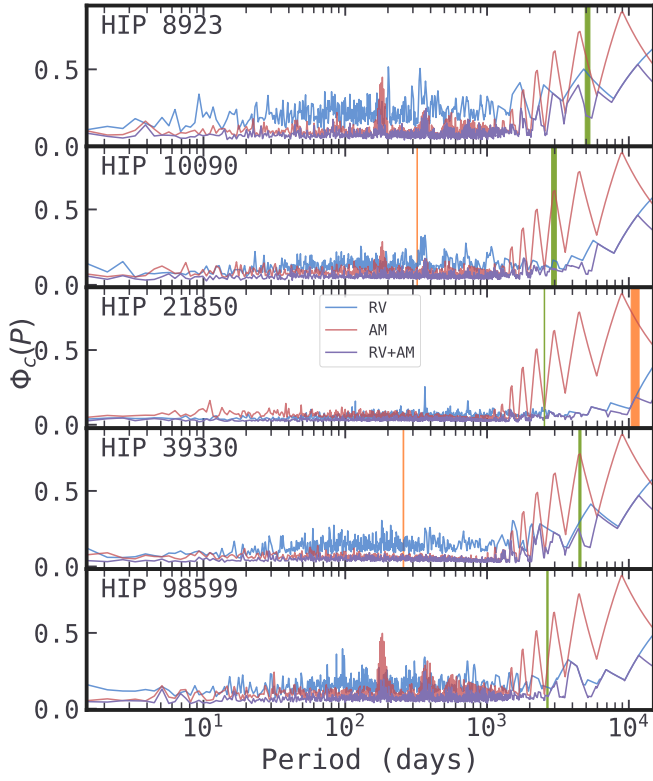


Fig. C.1. HIP 39330 corner plot of selected parameters, displaying a bimodal exploration.



**Fig. C.2.** Phase-coverage per system per data type. The y-axis shows phase-incompleteness  $\Phi_c(P)$  as a function of period, with 0 meaning no gaps, increasing up to 1 with gap-size. Blue solid line corresponds to the RV data phase-coverage, red line to astrometry data, and purple to both combined. Green and orange vertical bars display the best-fit orbital periods.

**Table C.1.** Measurements per instrument subset (counts).

Target	COR (07/14T/14)	HARPS (pre/15/20)	HIRES	AAT	RV total	IAD/GOST
HIP 8923	10/6/6	—/—/—	—	—	22	77/49
HIP 10090	12/3/6	32/4/—	—	—	57	106/52
HIP 21850	5/7/11	40/4/10	—	43	120	108/40
HIP 39330	10/7/10	22/3/—	—	—	52	132/44
HIP 98599	11/—/7	10/3/—	5	—	36	143/32

## Appendix D: Additional tables

Table D.3. HIP 98599 joint RV+astrometry parameter estimates.

Table D.1. HIP 8923 joint RV+astrometry parameter estimates.

Parameter	Prior	1 $\mathcal{K}$
Offsets and Jitter		
$\gamma_{C07}$ (m s <sup>-1</sup> )	$\sim\mathcal{U}(-200, 200)$	$-30.22^{+6.84}_{-2.18}$
$\gamma_{C14}$ (m s <sup>-1</sup> )	$\sim\mathcal{U}(-200, 200)$	$-38.17^{+2.18}_{-7.77}$
$\gamma_{C14T}$ (m s <sup>-1</sup> )	$\sim\mathcal{U}(-200, 200)$	$29.09^{+5.18}_{-2.66}$
$\sigma_{C07}$ (m s <sup>-1</sup> )	$\sim\mathcal{N}(0, 10)$	$1.71^{+1.89}_{-1.71}$
$\sigma_{C14}$ (m s <sup>-1</sup> )	$\sim\mathcal{N}(0, 5)$	$2.82^{+0.79}_{-0.27}$
$\sigma_{C14T}$ (m s <sup>-1</sup> )	$\sim\mathcal{N}(0, 10)$	$0.94^{+0.83}_{-0.94}$
Keplerian Orbit		
$P_1$ (days)	$\sim\mathcal{U}(1, 15000)$	$5160^{+150}_{-240}$
$K_1$ (m s <sup>-1</sup> )	$\sim\mathcal{U}(0, 200)$	$48.3^{+3.60}_{-5.5}$
$\phi_1$ (rad)	$\sim\mathcal{U}(0, 2\pi)$	$4.96^{+0.65}_{-0.72}$
$e_1$	$\sim\mathcal{N}(0, 0.3)$	$0.011^{+0.032}_{-0.011}$
$\omega_1$ (rad)	$\sim\mathcal{U}(0, 2\pi)$	$0.92^{+1.14}_{-0.56}$
$I_1$ (°)	$\sim\mathcal{I}(0, 180)$	$24.8^{+1.26}_{-3.9}$
$\Omega_1$ (°)	$\sim\mathcal{U}(0, 2\pi)$	$98.47^{+5.40}_{-8.12}$
Astrometry		
$\Delta\alpha_*$ (mas)	$\sim\mathcal{U}(-10, 10)$	$0.604^{+0.094}_{-0.009}$
$\Delta\delta$ (mas)	$\sim\mathcal{U}(-10, 10)$	$0.408^{+0.079}_{-0.068}$
$\Delta\varpi$ (mas)	$\sim\mathcal{U}(-10, 10)$	$0.017^{+0.017}_{-0.007}$
$\Delta\mu_{\alpha_*}$ (mas/yr)	$\sim\mathcal{U}(-10, 10)$	$0.220^{+0.021}_{-0.010}$
$\Delta\mu_{\delta}$ (mas/yr)	$\sim\mathcal{U}(-10, 10)$	$-0.237^{+0.013}_{-0.012}$
$J_{\text{hipp}}$ (mas)	$\sim\mathcal{U}(0, 10)$	$1.14^{+0.63}_{-0.60}$
$S_{\text{gaia}}$	$\sim\mathcal{N}(1, 1, 0.1)$	$1.02^{+0.02}_{-0.06}$

Parameter	Prior	1 $\mathcal{K}$
Offsets and Jitter		
$\gamma_{C07}$ (m s <sup>-1</sup> )	$\sim\mathcal{U}(-200, 200)$	$-42.12^{+2.61}_{-3.63}$
$\gamma_{C14}$ (m s <sup>-1</sup> )	$\sim\mathcal{U}(-200, 200)$	$15.58^{+2.82}_{-4.41}$
$\gamma_H$ (m s <sup>-1</sup> )	$\sim\mathcal{U}(-200, 200)$	$-1.09^{+1.58}_{-1.53}$
$\gamma_{\text{HIR}}$ (m s <sup>-1</sup> )	$\sim\mathcal{U}(-200, 200)$	$28.84^{+8.58}_{-9.66}$
$\gamma_{\text{H15}}$ (m s <sup>-1</sup> )	$\sim\mathcal{U}(-200, 200)$	$26.08^{+0.72}_{-2.45}$
$\sigma_{C07}$ (m s <sup>-1</sup> )	$\sim\mathcal{N}(0, 10)$	$3.63^{+3.41}_{-3.63}$
$\sigma_{C14}$ (m s <sup>-1</sup> )	$\sim\mathcal{N}(0, 5)$	$0.21^{+0.55}_{-0.21}$
$\sigma_H$ (m s <sup>-1</sup> )	$\sim\mathcal{N}(0, 5)$	$6.90^{+1.53}_{-0.27}$
$\sigma_{\text{HIR}}$ (m s <sup>-1</sup> )	$\sim\mathcal{N}(0, 10)$	$9.91^{+1.50}_{-1.59}$
$\sigma_{\text{H15}}$ (m s <sup>-1</sup> )	$\sim\mathcal{N}(0, 5)$	$2.56^{+1.52}_{-1.30}$
Keplerian Orbit		
$P_1$ (days)	$\sim\mathcal{U}(1, 10000)$	$2656^{+40}_{-16}$
$K_1$ (m s <sup>-1</sup> )	$\sim\mathcal{U}(0, 150)$	$45.53^{+1.04}_{-2.90}$
$\phi_1$ (rad)	$\sim\mathcal{U}(0, 2\pi)$	$5.47^{+0.25}_{-0.05}$
$e_1$	$\sim\mathcal{N}(0, 0.3)$	$0.169^{+0.002}_{-0.055}$
$\omega_1$ (rad)	$\sim\mathcal{U}(0, 2\pi)$	$4.80^{+0.06}_{-0.28}$
$I_1$ (°)	$\sim\mathcal{I}(0, 180)$	$29.7^{+6.9}_{-6.2}$
$\Omega_1$ (°)	$\sim\mathcal{U}(0, 2\pi)$	$302.26^{+7.55}_{-1.16}$
Astrometry		
$\Delta\alpha_*$ (mas)	$\sim\mathcal{U}(-10, 10)$	$-0.164^{+0.022}_{-0.020}$
$\Delta\delta$ (mas)	$\sim\mathcal{U}(-10, 10)$	$0.151^{+0.016}_{-0.043}$
$\Delta\varpi$ (mas)	$\sim\mathcal{U}(-10, 10)$	$-0.028^{+0.028}_{-0.023}$
$\Delta\mu_{\alpha_*}$ (mas/yr)	$\sim\mathcal{U}(-10, 10)$	$0.106^{+0.015}_{-0.008}$
$\Delta\mu_{\delta}$ (mas/yr)	$\sim\mathcal{U}(-10, 10)$	$0.138^{+0.016}_{-0.001}$
$J_{\text{hipp}}$ (mas)	$\sim\mathcal{U}(0, 10)$	$0.67^{+0.57}_{-0.50}$
$S_{\text{gaia}}$	$\sim\mathcal{N}(1, 1, 0.1)$	$1.24^{+0.03}_{-0.03}$

Table D.2. HIP 10090 joint RV+astrometry parameter estimates.

Parameter	Prior	1 $\mathcal{K}$	Parameter	Prior	1 $\mathcal{K}$
Offsets and Jitter			Astrometry		
$\gamma_{C07}$ (m s <sup>-1</sup> )	$\sim\mathcal{U}(-200, 200)$	$-24.98^{+6.37}_{-3.68}$	$\Delta\alpha_*$ (mas)	$\sim\mathcal{U}(-10, 10)$	$-0.158^{+0.049}_{-0.036}$
$\gamma_{C14T}$ (m s <sup>-1</sup> )	$\sim\mathcal{U}(-200, 200)$	$-4.08^{+7.19}_{-5.16}$	$\Delta\delta$ (mas)	$\sim\mathcal{U}(-10, 10)$	$0.013^{+0.030}_{-0.023}$
$\gamma_{C14}$ (m s <sup>-1</sup> )	$\sim\mathcal{U}(-200, 200)$	$7.43^{+7.80}_{-7.57}$	$\Delta\varpi$ (mas)	$\sim\mathcal{U}(-10, 10)$	$-0.003^{+0.013}_{-0.003}$
$\gamma_{\text{HIR}}$ (m s <sup>-1</sup> )	$\sim\mathcal{U}(-200, 200)$	$8.52^{+1.52}_{-1.64}$	$\Delta\mu_{\alpha_*}$ (mas/yr)	$\sim\mathcal{U}(-10, 10)$	$-0.059^{+0.016}_{-0.001}$
$\gamma_{\text{H15}}$ (m s <sup>-1</sup> )	$\sim\mathcal{U}(-200, 200)$	$-17.47^{+1.83}_{-0.65}$	$\Delta\mu_{\delta}$ (mas/yr)	$\sim\mathcal{U}(-10, 10)$	$-0.125^{+0.012}_{-0.010}$
$\sigma_{C07}$ (m s <sup>-1</sup> )	$\sim\mathcal{N}(0, 10)$	$2.52^{+2.08}_{-2.52}$	$J_{\text{hipp}}$ (mas)	$\sim\mathcal{U}(0, 10)$	$1.22^{+0.70}_{-0.13}$
$\sigma_{C14T}$ (m s <sup>-1</sup> )	$\sim\mathcal{N}(0, 10)$	$1.51^{+1.29}_{-1.15}$	$S_{\text{gaia}}$	$\sim\mathcal{N}(1, 0.1)$	$1.24^{+0.07}_{-0.07}$
$\sigma_{C14}$ (m s <sup>-1</sup> )	$\sim\mathcal{N}(0, 5)$	$4.40^{+2.91}_{-4.40}$			
$\sigma_{\text{HIR}}$ (m s <sup>-1</sup> )	$\sim\mathcal{N}(0, 5)$	$4.74^{+4.40}_{-0.23}$			
$\sigma_{\text{H15}}$ (m s <sup>-1</sup> )	$\sim\mathcal{N}(0, 5)$	$0.50^{+0.64}_{-0.50}$			
Keplerian Orbits					
$P_1$ (days)	$\sim\mathcal{U}(1, 10000)$	$2960^{+120}_{-100}$	$P_2$ (days)	$\sim\mathcal{U}(1, 10000)$	$321.82^{+0.32}_{-0.56}$
$K_1$ (m s <sup>-1</sup> )	$\sim\mathcal{U}(0, 100)$	$23.89^{+1.86}_{-2.86}$	$K_2$ (m s <sup>-1</sup> )	$\sim\mathcal{U}(0, 100)$	$11.76^{+1.00}_{-0.22}$
$\phi_1$ (rad)	$\sim\mathcal{U}(0, 2\pi)$	$2.88^{+0.19}_{-0.24}$	$\phi_2$ (rad)	$\sim\mathcal{U}(0, 2\pi)$	$4.45^{+0.44}_{-0.21}$
$e_1$	$\sim\mathcal{N}(0, 0.3)$	$0.115^{+0.005}_{-0.033}$	$e_2$	$\sim\mathcal{N}(0, 0.3)$	$0.188^{+0.043}_{-0.048}$
$\omega_1$ (rad)	$\sim\mathcal{U}(0, 2\pi)$	$1.82^{+0.32}_{-0.15}$	$\omega_2$ (rad)	$\sim\mathcal{U}(0, 2\pi)$	$4.94^{+0.24}_{-0.33}$
$I_1$ (°)	$\sim\mathcal{I}(0, 180)$	$156.5^{+1.8}_{-2.2}$	$I_2$ (°)	$\sim\mathcal{I}(0, 180)$	$153.8^{+1.3}_{-3.1}$
$\Omega_1$ (°)	$\sim\mathcal{U}(0, 2\pi)$	$341.63^{+4.04}_{-0.01}$	$\Omega_2$ (°)	$\sim\mathcal{U}(0, 2\pi)$	$341.87^{+2.99}_{-1.28}$

**Table D.4.** HIP 39330 joint RV+astrometry parameter estimates. Models  $2\mathcal{K}_1$  and  $2\mathcal{K}_2$  have different inclination priors.

Parameter	Prior	$2\mathcal{K}$	$2\mathcal{K}_1$	$2\mathcal{K}_2$
Offsets and Jitter				
$\gamma_{C07}$ (m s <sup>-1</sup> )	$\sim\mathcal{U}(-200, 200)$	14.29 <sup>+0.44</sup> <sub>-0.38</sub>	13.37 <sup>+3.55</sup> <sub>-3.70</sub>	16.64 <sup>+3.51</sup> <sub>-5.88</sub>
$\gamma_{C14}$ (m s <sup>-1</sup> )	$\sim\mathcal{U}(-200, 200)$	17.60 <sup>+0.45</sup> <sub>-4.10</sub>	14.76 <sup>+2.08</sup> <sub>-2.28</sub>	11.87 <sup>+2.77</sup> <sub>-1.46</sub>
$\gamma_{C14T}$ (m s <sup>-1</sup> )	$\sim\mathcal{U}(-200, 200)$	-5.42 <sup>+1.55</sup> <sub>-3.72</sub>	-6.95 <sup>+1.30</sup> <sub>-3.82</sub>	-0.57 <sup>+5.22</sup> <sub>-5.30</sub>
$\gamma_H$ (m s <sup>-1</sup> )	$\sim\mathcal{U}(-200, 200)$	8.95 <sup>+2.92</sup> <sub>-0.20</sub>	12.59 <sup>+3.15</sup> <sub>-3.64</sub>	8.35 <sup>+0.42</sup> <sub>-2.27</sub>
$\gamma_{H15}$ (m s <sup>-1</sup> )	$\sim\mathcal{U}(-200, 200)$	-13.16 <sup>+4.94</sup> <sub>-5.09</sub>	-16.84 <sup>+1.99</sup> <sub>-2.29</sub>	-13.76 <sup>+3.14</sup> <sub>-0.98</sub>
$\sigma_{C07}$ (m s <sup>-1</sup> )	$\sim\mathcal{N}(0, 10)$	2.30 <sup>+2.35</sup> <sub>-2.30</sub>	1.13 <sup>+0.68</sup> <sub>-1.13</sub>	1.82 <sup>+0.08</sup> <sub>-1.82</sub>
$\sigma_{C14}$ (m s <sup>-1</sup> )	$\sim\mathcal{N}(0, 5)$	3.69 <sup>+0.71</sup> <sub>-0.31</sub>	3.86 <sup>+0.85</sup> <sub>-0.28</sub>	3.45 <sup>+0.95</sup> <sub>-0.09</sub>
$\sigma_{C14T}$ (m s <sup>-1</sup> )	$\sim\mathcal{N}(0, 10)$	4.78 <sup>+3.03</sup> <sub>-4.77</sub>	3.98 <sup>+2.99</sup> <sub>-3.98</sub>	2.22 <sup>+0.18</sup> <sub>-2.21</sub>
$\sigma_H$ (m s <sup>-1</sup> )	$\sim\mathcal{N}(0, 5)$	5.09 <sup>+0.42</sup> <sub>-0.30</sub>	4.69 <sup>+0.90</sup> <sub>-0.78</sub>	4.93 <sup>+0.65</sup> <sub>-0.97</sub>
$\sigma_{H15}$ (m s <sup>-1</sup> )	$\sim\mathcal{N}(0, 5)$	3.56 <sup>+1.13</sup> <sub>-0.65</sub>	4.45 <sup>+0.48</sup> <sub>-1.40</sub>	2.82 <sup>+2.32</sup> <sub>-1.93</sub>
Keplerian Orbit				
$P_1$ (days)	$\sim\mathcal{U}(1, 10000)$	4596.9 <sup>+1.7</sup> <sub>-154.0</sub>	4654.2 <sup>+211.5</sup> <sub>-248.4</sub>	4490.5 <sup>+29.8</sup> <sub>-144.1</sub>
$K_1$ (m s <sup>-1</sup> )	$\sim\mathcal{U}(0, 100)$	20.96 <sup>+1.28</sup> <sub>-2.04</sub>	19.78 <sup>+1.25</sup> <sub>-1.80</sub>	18.28 <sup>+0.12</sup> <sub>-2.53</sub>
$\phi_1$ (rad)	$\sim\mathcal{U}(0, 2\pi)$	6.17 <sup>+0.16</sup> <sub>-0.51</sub>	5.05 <sup>+1.15</sup> <sub>-1.33</sub>	5.88 <sup>+0.40</sup> <sub>-0.08</sub>
$e_1$	$\sim\mathcal{N}(0, 0.3)$	0.109 <sup>+0.053</sup> <sub>-0.109</sub>	0.078 <sup>+0.053</sup> <sub>-0.078</sub>	0.064 <sup>+0.063</sup> <sub>-0.064</sub>
$\omega_1$ (rad)	$\sim\mathcal{U}(0, 2\pi)$	1.52 <sup>+0.71</sup> <sub>-0.17</sub>	2.85 <sup>+0.05</sup> <sub>-1.21</sub>	1.69 <sup>+0.23</sup> <sub>-0.41</sub>
$I_1$ (°)	$\sim\mathcal{I}(0, 180)$	110.10 <sup>+4.95</sup> <sub>-5.72</sub>	55.01 <sup>+0.55</sup> <sub>-3.86</sub>	127.14 <sup>+3.38</sup> <sub>-1.24</sub>
$\Omega_1$ (°)	$\sim\mathcal{U}(0, 2\pi)$	5.67 <sup>+4.91</sup> <sub>-5.22</sub>	253.32 <sup>+3.56</sup> <sub>-1.12</sub>	4.05 <sup>+4.96</sup> <sub>-5.05</sub>
$P_2$ (days)	$\sim\mathcal{U}(1, 10000)$	257.11 <sup>+1.55</sup> <sub>-1.41</sub>	258.34 <sup>+0.90</sup> <sub>-0.37</sub>	258.75 <sup>+0.29</sup> <sub>-0.99</sub>
$K_2$ (m s <sup>-1</sup> )	$\sim\mathcal{U}(0, 100)$	8.10 <sup>+1.56</sup> <sub>-1.31</sub>	9.73 <sup>+0.25</sup> <sub>-1.03</sub>	10.44 <sup>+1.41</sup> <sub>-1.72</sub>
$\phi_2$ (rad)	$\sim\mathcal{U}(0, 2\pi)$	3.45 <sup>+0.04</sup> <sub>-1.75</sub>	2.33 <sup>+1.24</sup> <sub>-0.35</sub>	3.08 <sup>+0.27</sup> <sub>-1.31</sub>
$e_2$	$\sim\mathcal{N}(0, 0.3)$	0.020 <sup>+0.002</sup> <sub>-0.020</sub>	0.079 <sup>+0.053</sup> <sub>-0.079</sub>	0.099 <sup>+0.053</sup> <sub>-0.099</sub>
$\omega_2$ (rad)	$\sim\mathcal{U}(0, 2\pi)$	2.69 <sup>+2.05</sup> <sub>-1.66</sub>	4.01 <sup>+0.52</sup> <sub>-1.08</sub>	3.32 <sup>+1.46</sup> <sub>-0.14</sub>
$I_2$ (°)	$\sim\mathcal{I}(0, 180)$	110.02 <sup>+5.13</sup> <sub>-5.31</sub>	53.77 <sup>+1.54</sup> <sub>-3.33</sub>	132.26 <sup>+1.44</sup> <sub>-3.46</sub>
$\Omega_2$ (°)	$\sim\mathcal{U}(0, 2\pi)$	1.67 <sup>+3.89</sup> <sub>-1.00</sub>	256.48 <sup>+3.68</sup> <sub>-1.21</sub>	5.96 <sup>+5.15</sup> <sub>-8.33</sub>
Astrometry				
$\Delta\alpha_*$ (mas)	$\sim\mathcal{U}(-10, 10)$	0.083 <sup>+0.029</sup> <sub>-0.045</sub>	-0.24 <sup>+0.056</sup> <sub>-0.053</sub>	0.143 <sup>+0.039</sup> <sub>-0.039</sub>
$\Delta\delta$ (mas)	$\sim\mathcal{U}(-10, 10)$	0.159 <sup>+0.052</sup> <sub>-0.050</sub>	0.006 <sup>+0.022</sup> <sub>-0.013</sub>	0.178 <sup>+0.020</sup> <sub>-0.027</sub>
$\Delta\varpi$ (mas)	$\sim\mathcal{U}(-10, 10)$	-0.005 <sup>+0.015</sup> <sub>-0.001</sub>	0.006 <sup>+0.004</sup> <sub>-0.013</sub>	0.009 <sup>+0.003</sup> <sub>-0.013</sub>
$\Delta\mu_{\alpha_*}$ (mas/yr)	$\sim\mathcal{U}(-10, 10)$	0.005 <sup>+0.012</sup> <sub>-0.016</sub>	-0.034 <sup>+0.013</sup> <sub>-0.012</sub>	-0.008 <sup>+0.002</sup> <sub>-0.010</sub>
$\Delta\mu_\delta$ (mas/yr)	$\sim\mathcal{U}(-10, 10)$	0.057 <sup>+0.002</sup> <sub>-0.009</sub>	0.054 <sup>+0.003</sup> <sub>-0.010</sub>	0.067 <sup>+0.012</sup> <sub>-0.017</sub>
$J_{\text{hipp}}$ (mas)	$\sim\mathcal{U}(0, 10)$	0.16 <sup>+0.12</sup> <sub>-0.16</sub>	0.60 <sup>+0.33</sup> <sub>-0.60</sub>	0.70 <sup>+0.32</sup> <sub>-0.70</sub>
$S_{\text{gaia}}$	$\sim\mathcal{N}(1, 0.1)$	1.24 <sup>+0.11</sup> <sub>-0.07</sub>	1.32 <sup>+0.03</sup> <sub>-0.04</sub>	1.30 <sup>+0.06</sup> <sub>-0.01</sub>

**Table D.5.** Planet signatures summary, with Jupiter analogues in bold.

Planet	Period (days)		Mass ( $M_J$ )		Semi-major axis (AU)	
	RV	RV+AM	RV	RV+AM	RV	RV+AM
HIP 8923b	5116 <sup>+456</sup> <sub>-259</sub>	5160 <sup>+150</sup> <sub>-240</sub>	4.30 <sup>+0.07</sup> <sub>-0.75</sub>	9.98 <sup>+0.78</sup> <sub>-0.16</sub>	5.89 <sup>+0.30</sup> <sub>-0.26</sub>	5.90 <sup>+0.10</sup> <sub>-0.22</sub>
HIP 10090b	2975 <sup>+139</sup> <sub>-97</sub>	2960 <sup>+120</sup> <sub>-100</sub>	3.95 <sup>+0.14</sup> <sub>-0.10</sub>	3.87 <sup>+0.65</sup> <sub>-0.60</sub>	1.53 <sup>+0.12</sup> <sub>-0.14</sub>	3.87 <sup>+0.19</sup> <sub>-0.11</sub>
HIP 10090c	321.3 <sup>+0.5</sup> <sub>-0.4</sub>	321.8 <sup>+0.3</sup> <sub>-0.6</sub>	0.39 <sup>+0.02</sup> <sub>-0.03</sub>	0.85 <sup>+0.03</sup> <sub>-0.12</sub>	0.87 <sup>+0.03</sup> <sub>-0.01</sub>	0.90 <sup>+0.01</sup> <sub>-0.01</sub>
HIP 21850b	2540 <sup>+4</sup> <sub>-5</sub>	2539 <sup>+1</sup> <sub>-3</sub>	8.21 <sup>+0.13</sup> <sub>-0.46</sub>	8.25 <sup>+1.05</sup> <sub>-0.85</sub>	3.65 <sup>+0.02</sup> <sub>-0.11</sub>	3.49 <sup>+0.18</sup> <sub>-0.14</sub>
HIP 21850c	15903 <sup>+2470</sup> <sub>-4840</sub>	11320 <sup>+490</sup> <sub>-940</sub>	6.62 <sup>+1.37</sup> <sub>-2.46</sub>	4.67 <sup>+0.44</sup> <sub>-0.43</sub>	12.45 <sup>+1.40</sup> <sub>-2.71</sub>	9.90 <sup>+0.29</sup> <sub>-0.62</sub>
HIP 39330b	4636 <sup>+300</sup> <sub>-197</sub>	4650 <sup>+210</sup> <sub>-250</sub>	2.59 <sup>+0.51</sup> <sub>-0.07</sub>	1.67 <sup>+0.19</sup> <sub>-0.08</sub>	5.43 <sup>+0.16</sup> <sub>-0.17</sub>	5.05 <sup>+0.23</sup> <sub>-0.17</sub>
HIP 98599b	2579 <sup>+79</sup> <sub>-90</sub>	2656 <sup>+40</sup> <sub>-16</sub>	3.28 <sup>+0.17</sup> <sub>-0.13</sub>	6.85 <sup>+0.10</sup> <sub>-0.22</sub>	3.95 <sup>+0.03</sup> <sub>-0.05</sub>	3.96 <sup>+0.07</sup> <sub>-0.01</sub>